CORONAVIRUS

Non-neuronal expression of SARS-CoV-2 entry genes in the olfactory system suggests mechanisms underlying COVID-19–associated anosmia

Copyright © 2020 The Authors, some rights reserved; exclusive licensee American Association for the Advancement of Science. No claim to original U.S. Government Works. Distributed under a Creative Commons Attribution License 4.0 (CC BY).

David H. Brann[1]*, Tatsuya Tsukahara[1]*, Caleb Weinreb[1]*, Marcela Lipovsek[2], Koen Van den Berge[3,4], Boying Gong[5], Rebecca Chance[6], Iain C. Macaulay[7], Hsin-Jung Chou[6], Russell B. Fletcher[6†], Diya Das[6,8‡], Kelly Street[9,10], Hector Roux de Bezieux[5,11], Yoon Gi Choi[12], Davide Risso[13], Sandrine Dudoit[3,5], Elizabeth Purdom[3], Jonathan Mill[14], Ralph Abi Hachem[15], Hiroaki Matsunami[16], Darren W. Logan[17], Bradley J. Goldstein[15], Matthew S. Grubb[2], John Ngai[6,12,18§], Sandeep Robert Datta[1]‖

Altered olfactory function is a common symptom of COVID-19 (coronavirus disease 2019), but its etiology is unknown. A key question is whether SARS-CoV-2 (severe acute respiratory syndrome coronavirus 2; CoV-2)—the causal agent in COVID-19—affects olfaction directly, by infecting olfactory sensory neurons or their targets in the olfactory bulb, or indirectly, by perturbing support cells. Bulk and single-cell RNA sequencing revealed that support and stem cells in the human and mouse olfactory epithelium and vascular pericytes in the mouse olfactory bulb express angiotensin-converting enzyme 2 (ACE2), which is essential for CoV-2 cell entry. In contrast, ACE2 was not detected in either olfactory sensory neurons or olfactory bulb neurons. Immunostaining confirmed these results and revealed pervasive expression of ACE2 protein in dorsally located olfactory epithelial sustentacular cells and mouse olfactory bulb pericytes. These findings suggest that CoV-2 infection of non-neuronal cell types leads to olfactory dysfunction in patients with COVID-19.

INTRODUCTION

SARS-CoV-2 (severe acute respiratory syndrome coronavirus 2; CoV-2) is a pandemic coronavirus that causes the COVID-19 (coronavirus disease 2019) syndrome, which can include upper respiratory infection (URI) symptoms, severe respiratory distress, acute cardiac injury, and death (*1*–*4*). CoV-2 is closely related to other coronaviruses, including the causal agents in pandemic SARS and MERS (Middle East respiratory syndrome) (SARS-CoV and MERS-CoV, respectively) and endemic viruses typically associated with mild URI syndromes (HCoV-OC43, HCoV-HKU1, HCoV-229E, and HCoV-NL63) (*5*–*7*). Clinical reports suggest that infection with CoV-2 is associated with high rates of disturbances in smell and taste perception, including anosmia (*8*–*13*). While many viruses (including coronaviruses) induce transient changes in odor perception due to inflammatory responses, in at least some cases, COVID-19–related anosmia has been reported to occur in the absence of significant nasal inflammation or coryzal symptoms (*11*, *14*–*16*). Furthermore, recovery from COVID-19–related anosmia often occurs over weeks (*11*, *17*, *18*), while recovery from typical postviral anosmia—which is often caused by direct damage to olfactory sensory neurons (OSNs)—frequently takes months (*19*–*21*). These observations suggest that CoV-2 might target odor processing through mechanisms distinct from those used by other viruses, although the specific means through which CoV-2 alters odor perception remains unknown.

CoV-2—like SARS-CoV—infects cells through interactions between its spike (S) protein and the angiotensin-converting enzyme 2 (ACE2) protein on target cells. This interaction requires cleavage of the S protein, likely by the cell surface protease TMPRSS2 (transmembrane serine protease 2), although other proteases [such as cathepsin B and L (CTSB/CTSL)] may also be involved (*4*–*6*, *22*–*25*). Other coronaviruses use different cell surface receptors and proteases to facilitate cellular entry, including DPP4, FURIN, and HSPA5 for MERS-CoV; ANPEP for HCoV-229E; TMPRSS11D for SARS-CoV (in addition to ACE2 and TMPRSS2); and ST6GAL1 and ST3GAL4 for HCoV-OC43 and HCoV-HKU1 (*6*, *26*–*28*).

We hypothesized that identifying the specific cell types susceptible to direct CoV-2 infection (due to, e.g., ACE2 and TMPRSS2 expression) would provide insight into possible mechanisms through which COVID-19 alters smell perception. The nasal epithelium is divided into a respiratory epithelium (RE) and olfactory epithelium

[1]Harvard Medical School Department of Neurobiology, Boston, MA 02115, USA. [2]Centre for Developmental Neurobiology, Institute of Psychiatry, Psychology and Neuroscience (IoPPN), King's College London, London SE1 1UL, UK. [3]Department of Statistics, University of California, Berkeley, Berkeley, CA 94720, USA. [4]Department of Applied Mathematics, Computer Science and Statistics, Ghent University, Ghent, Belgium. [5]Division of Biostatistics, School of Public Health, University of California, Berkeley, Berkeley, CA 94720, USA. [6]Department of Molecular and Cell Biology, University of California, Berkeley, Berkeley, CA 94720, USA. [7]Earlham Institute, Norwich Research Park, Norwich NR4 7UZ, UK. [8]Berkeley Institute for Data Science, University of California, Berkeley, Berkeley, CA 94720, USA. [9]Department of Data Sciences, Dana-Farber Cancer Institute, Boston, MA 02115, USA. [10]Department of Biostatistics, Harvard T.H. Chan School of Public Health, Boston, MA 02115, USA. [11]Center for Computational Biology, University of California, Berkeley, Berkeley, CA 94720, USA. [12]QB3 Functional Genomics Laboratory, University of California, Berkeley, Berkeley, CA 94720, USA. [13]Department of Statistical Sciences, University of Padova, Padova, Italy. [14]University of Exeter Medical School, College of Medicine and Health, University of Exeter, Exeter EX2 5DW, UK. [15]Department of Head and Neck Surgery and Communication Sciences, Duke University School of Medicine, Durham, NC 27717, USA. [16]Department of Molecular Genetics and Microbiology, Department of Neurobiology, Duke University School of Medicine, Duke Institute for Brain Sciences, Durham, NC 27710, USA. [17]Waltham Petcare Science Institute, Leicestershire LE14 4RT, UK. [18]Helen Wills Neuroscience Institute, University of California, Berkeley, Berkeley, CA 94720, USA.
*These authors contributed equally to this work.
†Present address: Surrozen Inc., South San Francisco, CA 94080, USA.
‡Present address: Genentech Inc., South San Francisco, CA 94080, USA.
§Present address: National Institute of Neurological Disorders and Stroke, National Institutes of Health, Bethesda, MD 20892, USA.
‖Corresponding author. Email: srdatta@hms.harvard.edu

Downloaded from http://advances.sciencemag.org/ on October 30, 2020

(OE), whose functions and cell types differ. The nasal RE is continuous with the epithelium that lines much of the respiratory tract and is thought to humidify air as it enters the nose; main cell types include basal cells, ciliated cells, secretory cells (including goblet cells), and brush/microvillar (MV) cells (Fig. 1) (*29*, *30*). The OE, in contrast, is responsible for odor detection, as it houses mature OSNs (mOSNs) that interact with odors via receptors localized on their dendritic cilia. OSNs are supported by sustentacular (SUS) cells, which act to structurally support sensory neurons and phagocytose and/or detoxify potentially damaging agents, and maintain local salt and water balance (*31*–*33*); MV cells and mucus-secreting Bowman's gland (BG) cells also play important roles in maintaining OE homeostasis and function (Fig. 1) (*29*, *34*). In addition, the OE contains globose basal cells (GBCs), which are primarily responsible for regenerating OSNs during normal epithelial turnover, and horizontal basal cells (HBCs), which are reserve stem cells activated upon tissue damage (*35*–*37*). Although studies defining the lineage relationships between GBCs, HBCs, and their progeny have necessarily been performed in rodents, basal progenitor populations with similar transcriptional profiles are present in adult human OE, suggesting closely related homeostatic and injury-response mechanisms (*37*, *38*). Odor information is conveyed from the OE to the brain by OSN axons, which puncture the cribriform plate at the base of the skull and terminate in the olfactory bulb (OB). Within the OB, local circuits process olfactory information before sending it to higher brain centers (Fig. 1).

It has recently been demonstrated through single-cell RNA sequencing (RNA-seq) analysis (referred to herein as scSeq) that cells from the human upper airway—including nasal RE goblet and ciliated cells—express high levels of *ACE2* and *TMPRSS2*, suggesting that these RE cell types may serve as a viral reservoir during CoV-2 infection (*39*, *40*). However, analyzed samples in these datasets did not include any OSNs or SUS cells, indicating that tissue sampling in these experiments did not include the OE (*41*, *42*). Here, we query both new and previously published bulk RNA-seq and scSeq datasets from the olfactory system for expression of *ACE2*, *TMPRSS2*, and other genes implicated in coronavirus entry. We find that non-neuronal cells in the OE and OB, including support, stem, and perivascular cells, express CoV-2 entry–associated transcripts and their associated proteins, suggesting that infection of these non-neuronal cell types contributes to anosmia in patients with COVID-19.

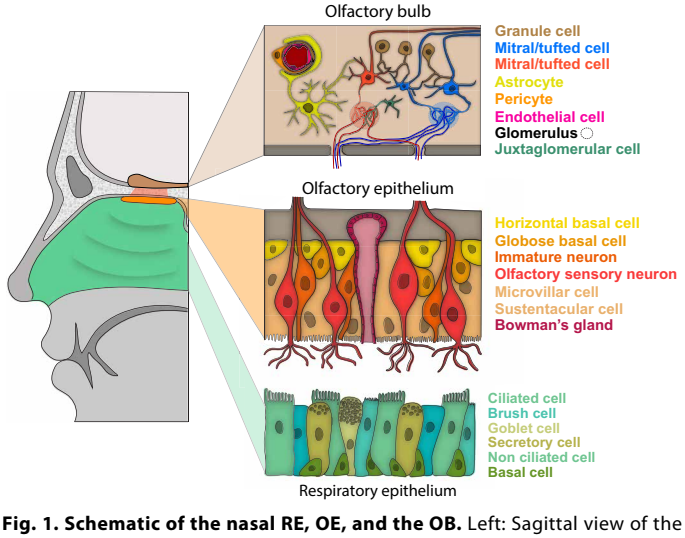

Fig. 1. Schematic of the nasal RE, OE, and the OB. Left: Sagittal view of the human nasal cavity, in which respiratory and olfactory epithelia are colored. Right: For each type of epithelium, a schematic of the anatomy and known major cell types are shown. In the OB in the brain (tan), the axons from OSNs coalesce into glomeruli, and mitral/tufted cells innervate these glomeruli and send olfactory projections to downstream olfactory areas. Glomeruli are also innervated by juxtaglomerular cells, a subset of which are dopaminergic.

RESULTS

Expression of CoV-2 entry genes in human OE

To determine whether genes relevant to CoV-2 entry are expressed in OSNs or other cell types in the human OE, we queried previously published bulk RNA-seq data derived from the whole olfactory mucosa (WOM) of macaque, marmoset, and human (*43*) and found expression of almost all CoV-2 entry–related genes in all WOM samples (fig. S1A). To identify the specific cell types in human OE that express *ACE2*, we quantified gene expression in scSeq derived from four human nasal biopsy samples recently reported by Durante *et al.* (*38*). Neither *ACE2* nor *TMPRSS2* was detected in mOSNs, whereas these genes were detected in both SUS cells and HBCs (Fig. 2, A to D, and fig. S1, B to E). In contrast, genes relevant to cell entry of other CoVs were expressed in OSNs, as well as in other OE cell types. We confirmed the expression of ACE2 protein via immunostaining of human OE biopsy tissue, which revealed expression in SUS and HBC cells, and an absence of ACE2 protein in OSNs (Fig. 2E and fig. S2). Together, these results demonstrate that SUS and olfactory stem cells, but not OSNs, are potentially direct targets of CoV-2 in the human OE.

Given that the nasopharynx is a major site of infection for CoV-2 (*10*), we compared the frequency of *ACE2* and *TMPRSS2* expression among the cell types in the human RE and OE (*38*). SUS cells exhibited the highest frequency of *ACE2* expression in the OE (2.9% of cells), although this frequency was slightly lower than that observed in respiratory ciliated and secretory cells (3.6 and 3.9%, respectively). While all HBC subtypes expressed *ACE2*, the frequency of expression of *ACE2* was lower in olfactory HBCs (0.8% of cells) compared to respiratory HBCs (1.7% of cells) (Fig. 2D). In addition, all other RE cell subtypes showed higher frequencies of *ACE2* and *TMPRSS2* expression than was apparent in OE cells.

These results demonstrate the presence of key CoV-2 entry–related genes in specific cell types in the OE but at lower levels of expression than in RE isolated from the human nasal mucosa. We wondered whether these lower levels of expression might nonetheless be sufficient for infection by CoV-2. It was recently reported that the nasal RE has higher expression of CoV-2 entry genes than the RE that lines the trachea or lungs (*44*), and we therefore asked where the OE fell within this previously established spectrum of expression. To address this question, we developed a two-step alignment procedure in which we first sought to identify cell types that were common across the OE and RE and then leveraged gene expression patterns in these common cell types to normalize gene expression levels across all cell types in the OE and RE (Fig. 3 and fig. S3). This approach revealed correspondences between submucosal gland goblet cells in the RE and BG cells in the OE (96% mapping probability; see Materials and Methods) and between pulmonary ionocytes in the RE and a subset of MV cells in the OE (99% mapping

Downloaded from http://advances.sciencemag.org/ on October 30, 2020

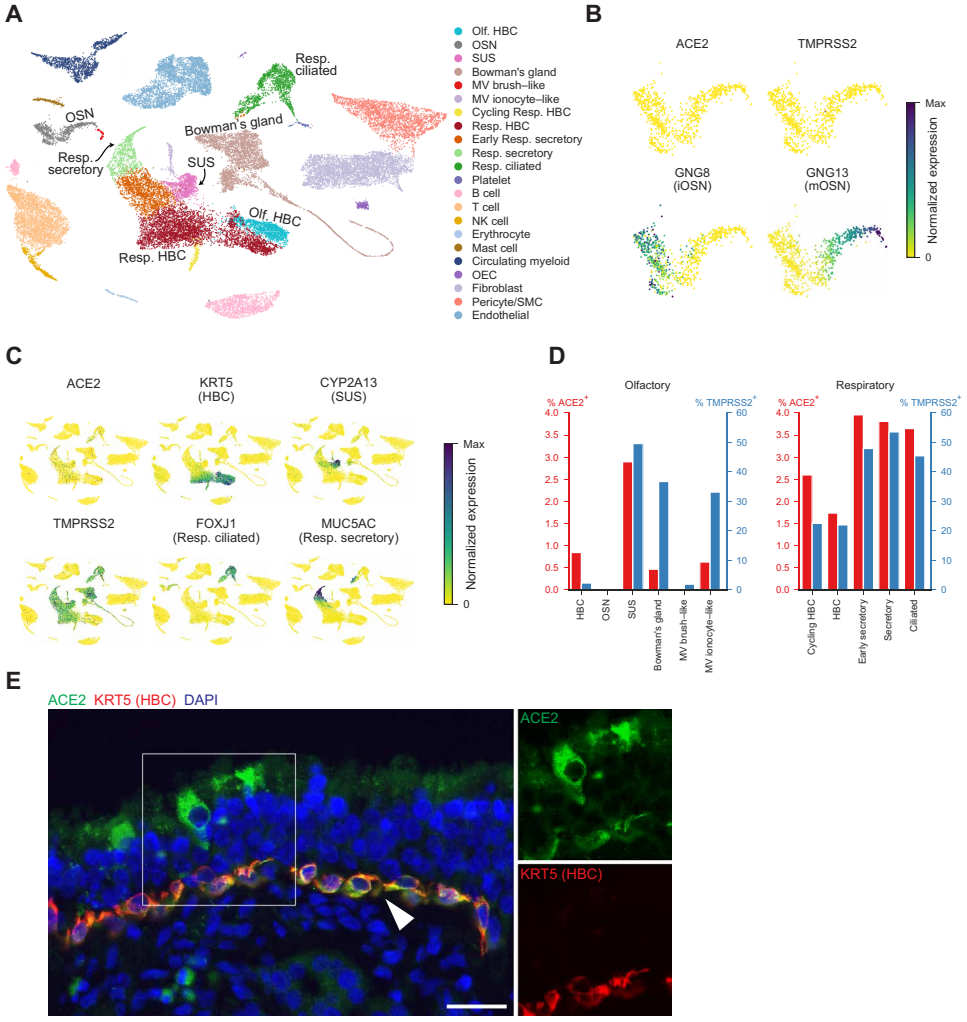

Fig. 2. Coronavirus cell entry–related genes are expressed in human RE and OE but are not detected in human OSNs. (**A**) UMAP representation of cell types in human nasal biopsy scSeq data from Durante *et al.* (*38*). Each dot represents an individual cell, colored by cell type. Resp., respiratory; OEC, olfactory ensheathing cell; SMC, smooth muscle cell; NK, natural killer. (**B**) UMAP representations of 865 detected immature (*GNG8*) and mature (*GNG13*) OSNs. Neither *ACE2* nor *TMPRSS2* is detected in either population of OSNs. The color represents the normalized expression level for each gene (number of UMIs for a given gene divided by the total number of UMIs for each cell). (**C**) UMAP representations of all cells, depicting the normalized expression of CoV-2–related genes *ACE2* and *TMPRSS2*, as well as several cell-type markers. *ACE2* and *TMPRSS2* are expressed in respiratory and olfactory cell types but not in OSNs. *ACE2* and *TMPRSS2* are detected in HBC (*KRT5*) and SUS (*CYP2A13*) cells, as well as other respiratory epithelial cell types, including respiratory ciliated (*FOXJ1*) cells. (**D**) Percentage of cells expressing *ACE2* and *TMPRSS2*. *ACE2* was not detected in any OSNs, but was observed in SUS cells and HBCs, among other olfactory and respiratory epithelial cell types. Olfactory and respiratory cell types are shown separately. *ACE2* and *TMPRSS2* were also significantly coexpressed (odds ratio, 7.088; $P = 3.74 \times 10^{-57}$, Fisher's exact test). (**E**) ACE2 immunostaining of a human olfactory mucosal biopsy (taken from a 28-year-old female). ACE2 protein (green) is detected in SUS cells and KRT5-positive HBCs (red; white arrowhead). Nuclei were stained with 4′,6-diamidino-2-phenylindole (DAPI) (blue). Scale bar, 25 μm. The ACE2 and KRT5 channels from the box on the left are shown individually on the right.

probability; see Materials and Methods and fig. S3); after alignment, human OE SUS cells were found to express *ACE2* and *TMPRSS2* at levels similar to those observed in the remainder of the non-nasal respiratory tract (Fig. 3C) (*44*). As CoV-2 can infect cells in the lower respiratory tract (*40*, *45*), these results are consistent with the possibility that specific cell types in the human OE express *ACE2* at a level that is permissive for direct infection.

Expression of CoV-2 entry genes in mouse OE

To further explore the distribution of CoV-2 cell entry genes in the olfactory system, we turned to the mouse, which enables interrogative experiments not possible in humans. To evaluate whether mouse expression patterns correspond to those observed in the human OE, we examined published datasets in which RNA-seq was independently performed on mouse WOM and on purified populations of mOSNs (*46*–*48*). The CoV-2 receptor *Ace2* and the protease *Tmprss2* were expressed in WOM, as were the cathepsins *Ctsb* and *Ctsl* (Fig. 4A and fig. S4A) (*46*). However, expression of these genes (with the exception of *Ctsb*) was much lower, and *Ace2* expression was nearly absent in purified OSN samples (Fig. 4A and fig. S4A, see legend for counts). Genes used for cell entry by other CoVs (except *St3gal4*) were also expressed in WOM, and de-enriched in purified OSNs. The de-enrichment of *Ace2* and *Tmprss2* in OSNs relative to WOM was also observed in two other mouse RNA-seq datasets (fig. S4B) (*47*, *48*).

Downloaded from http://advances.sciencemag.org/ on October 30, 2020

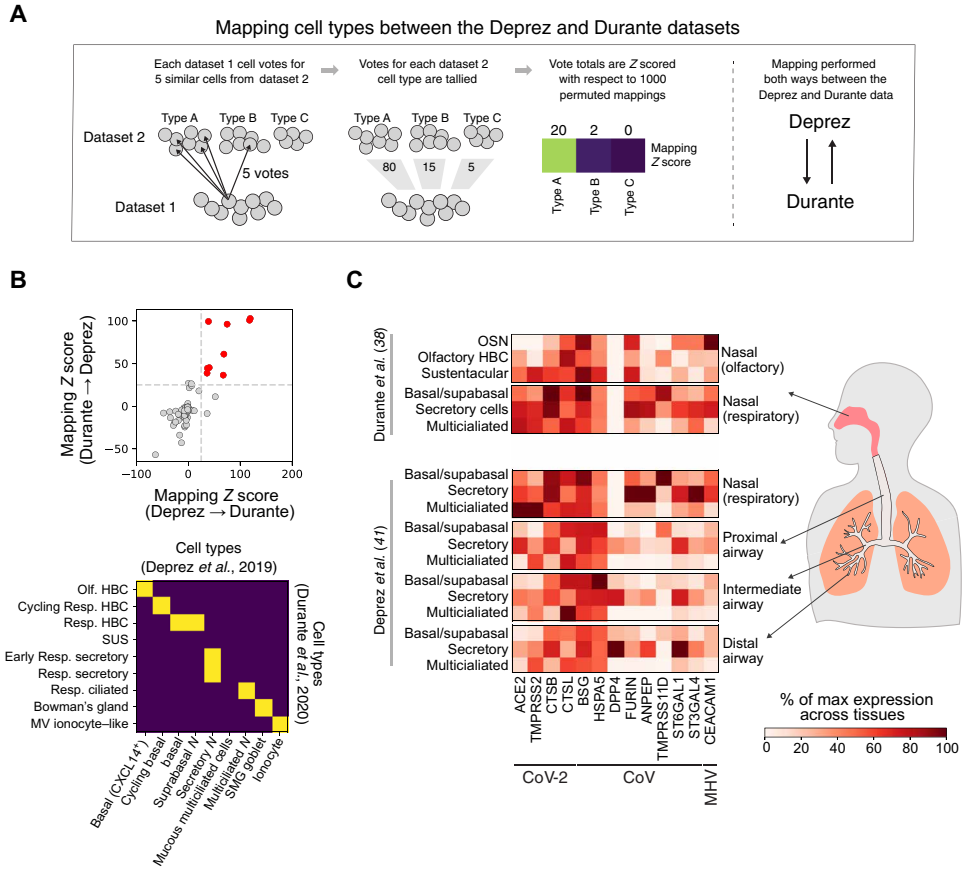

Fig. 3. Coronavirus cell entry–related genes are expressed at comparable levels across respiratory and olfactory epithelial datasets. (**A**) Schematic of the mapping strategy used to identify similar cell types across datasets, applied to a toy example. Each cell type from dataset 1 is mapped to cell types from dataset 2. From left to right: Each dataset 1 cell voted on its five most similar cells in dataset 2; the total number of votes cast for each dataset 2 cell type was quantified; and vote totals were *Z*-scored against 1000 shuffles where cell-type labels were permutated. (**B**) Mapping was performed bidirectionally between the Deprez *et al.* (*41*) and Durante *et al.* (*38*) datasets, and the mapping *Z* scores in each direction are compared. Top: The set of cell-type correspondences with high *Z* scores (>25) in both directions are colored red. Bottom: The set of cell-type correspondences with high bidirectional mappings shown in red in top panel are highlighted in yellow. (**C**) Gene expression across cell types and tissues in Durante *et al.* (top) and Deprez *et al.* (bottom). Each gene is normalized to its maximum value across all tissues. Gene expression from Durante *et al.* was normalized to that in Deprez *et al.* to enable comparisons (see Materials and Methods and fig. S3). The tissues correspond to the indicated positions along the airway from nasal to distal lung. *ACE2* expression in olfactory HBC and SUS cells is comparable to that observed in other cell types in the lower respiratory tract.

The presence of *Ace2* and *Tmprss2* transcripts in mouse WOM and their (near total) absence in purified OSNs suggest that the molecular components that enable CoV-2 entry into cells are expressed in non-neuronal cell types in the mouse nasal epithelium. To identify the specific cell types that express *Ace2* and *Tmprss2*, we performed scSeq (via Drop-seq; see Materials and Methods) on mouse WOM (Fig. 4B). These results were consistent with observations made in the human epithelium: *Ace2* and *Tmprss2* were expressed in a fraction of SUS and BG cells and a very small fraction of stem cells but not in OSNs (zero of 17,666 identified mOSNs; Fig. 4C and fig. S4, C and D). Of note, only dorsally located SUS cells, which express the markers *Sult1c1* and *Acsm4*, were positive for *Ace2* (Fig. 4D and fig. S4, D and E). Based upon this observation, we reanalyzed the human OE scSeq data, which revealed that all positive SUS cells expressed genetic markers associated with the dorsal epithelium (fig. S1D). An independent mouse scSeq dataset (obtained using the 10x Chromium platform; see Materials and Methods) confirmed that OSNs did not express *Ace2* (2 of 28,769 mOSNs were positive for *Ace2*), while expression was observed in a fraction of BG cells and HBCs (fig. S5 and see Materials and Methods). Expression in SUS cells was not observed in this dataset, which included relatively few dorsal SUS cells (a possible consequence of the specific cell isolation procedure associated with the 10x Chromium platform; compare fig. S5C and Fig. 4D).

Staining of the mouse WOM with anti-ACE2 antibodies confirmed that ACE2 protein is expressed in SUS cells and is specifically localized to the SUS cell microvilli (Fig. 5). ACE2$^+$ SUS cells were identified exclusively within the dorsal subregion of the OE; critically, within that region, many (and possibly all) SUS cells expressed ACE2 (Fig. 5, B to E). Staining was also observed in BG cells, but not in OSNs, and in subsets of RE cells (Fig. 5, F and G). Together, these data demonstrate that ACE2 is expressed by SUS cells that specifically reside in the dorsal epithelium in both mouse and human.

Expression of CoV-2 entry genes in injured mouse OE

Viral injury can lead to broad changes in OE physiology that are accompanied by recruitment of stem cell populations tasked

Downloaded from http://advances.sciencemag.org/ on October 30, 2020

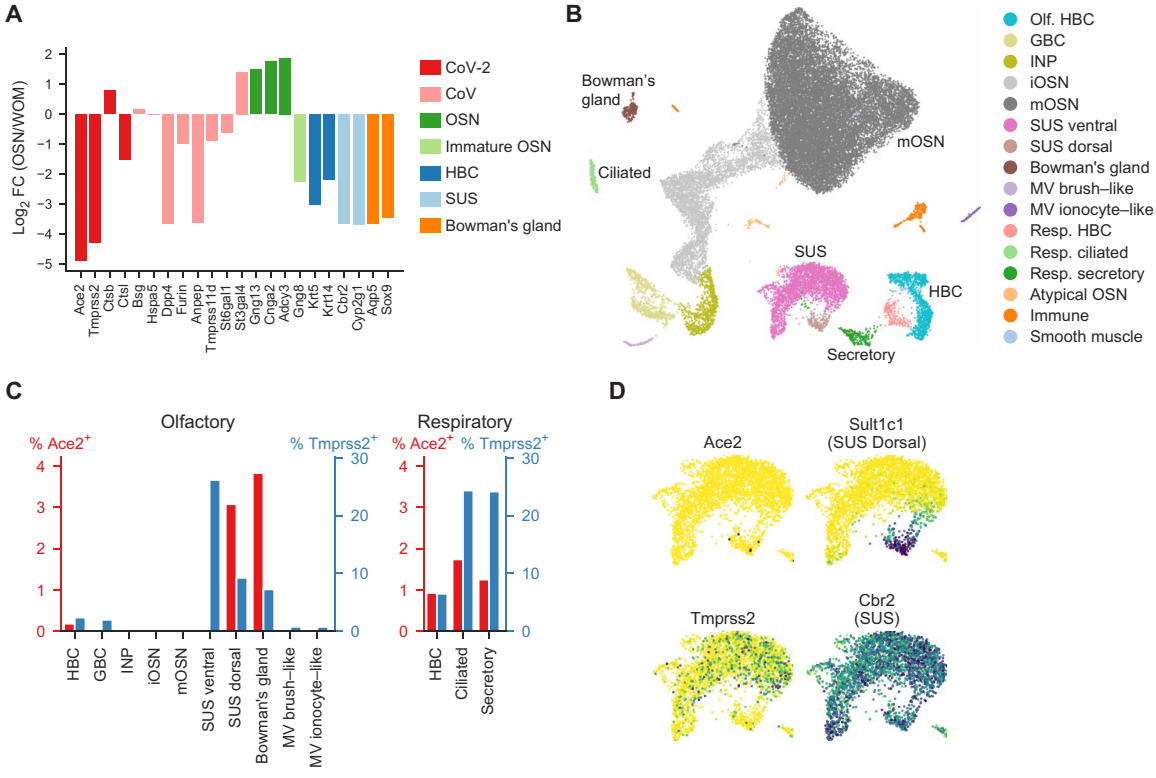

Fig. 4. ACE2 is expressed in the mouse nasal epithelium but not in OSNs. (**A**) Log_2 fold change (FC) in mean across-replicate gene expression between OSNs and WOM for CoV-related genes and cell-type markers, data from Saraiva *et al.* (*46*). (**B**) UMAP representation of scSeq data from the WOM, colored by cell types. INP, immediate neural precursor. (**C**) Percentage of cells expressing *Ace2* and *Tmprss2* in olfactory and respiratory cell types in the WOM (Drop-seq) dataset. Detection was considered positive if any transcripts (UMIs) were expressed for a given gene. SUS cells from dorsal and ventral zones are quantified separately. *Ace2* is detected in dorsal SUS, BG, HBCs, and respiratory cell types. (**D**) UMAP representation of SUS cells, with expression of CoV-2–related genes *Ace2* and *Tmprss2*, as well as marker genes for SUS (both pan-SUS marker *Cbr2* and dorsal-specific marker *Sult1c1*) indicated. The color represents the normalized expression level for each gene (number of UMIs for a given gene divided by the total number of UMIs for each cell; in this plot, *Ace2* expression is binarized for visualization purposes). *Ace2*$^+$ SUS cells are found within the dorsal *Sult1c1*$^+$ subset. UMAP plots for other cell types are shown in fig. S4.

with regenerating the epithelium (*35*, *37*, *49*). To characterize the distribution of *Ace2* expression under similar circumstances, we injured the OE by treating mice with methimazole (which ablates both support cells and OSNs) and then used a previously established lineage-tracing protocol to perform scSeq on HBCs and their descendants during subsequent regeneration (see Materials and Methods) (*36*). This analysis revealed that after injury, *Ace2* and *Tmprss2* are expressed in subsets of SUS cells and HBCs, as well as in the activated HBCs that serve to regenerate the epithelium (Fig. 6, A to C, and fig. S6A; note that activated HBCs express *Ace2* at higher levels than resting HBCs). Analysis of the *Ace2*$^+$ SUS cell population revealed expression of dorsal epithelial markers (Fig. 6D). To validate these results, we reanalyzed a similar lineage-tracing dataset in which identified HBCs, and their progeny were subject to Smart-seq2–based deep sequencing, which is more sensitive than droplet-based scSeq methods (*36*). In this dataset, *Ace2* was detected in more than 0.7% of GBCs, nearly 2% of activated HBCs and nearly 3% of SUS cells, but was not detected in OSNs (fig. S6B). Immunostaining with anti-ACE2 antibodies confirmed that ACE2 protein was present in activated stem cells under these regeneration conditions (Fig. 6E). These results demonstrate that activated stem cells recruited during injury express ACE2 and do so at higher levels than those in resting stem cells.

Expression of CoV-2 entry genes in mouse OB

Given the potential for the RE and OE in the nasal cavity to be directly infected with CoV-2, we assessed the expression of *Ace2* and other CoV-2 entry genes in the mouse OB, which is directly connected to OSNs via cranial nerve I (CN I); in principle, alterations in OB function could cause anosmia independently of functional changes in the OE. To do so, we performed scSeq (using Drop-seq; see Materials and Methods) on the mouse OB and merged these data with a previously published OB scSeq analysis, yielding a dataset with nearly 50,000 single cells (see Materials and Methods) (*50*). This analysis revealed that *Ace2* expression was absent from OB neurons and, instead, was observed only in vascular cells, predominantly in pericytes, which are involved in blood pressure regulation, maintenance of the blood-brain barrier, and inflammatory responses (Fig. 7, A to D, and figs. S7 and S8) (*51*). Although other potential CoV proteases were expressed in the OB, *Tmprss2* was not expressed.

We also performed Smart-seq2–based deep sequencing of single OB dopaminergic juxtaglomerular neurons, a population of local interneurons in the OB glomerular layer that (similar to tufted cells) can receive direct monosynaptic input from nasal OSNs (Fig. 7E, fig. S9, and see Materials and Methods); these experiments confirmed the virtual absence of *Ace2* and *Tmprss2* expression in this cell type.

Downloaded from http://advances.sciencemag.org/ on October 30, 2020

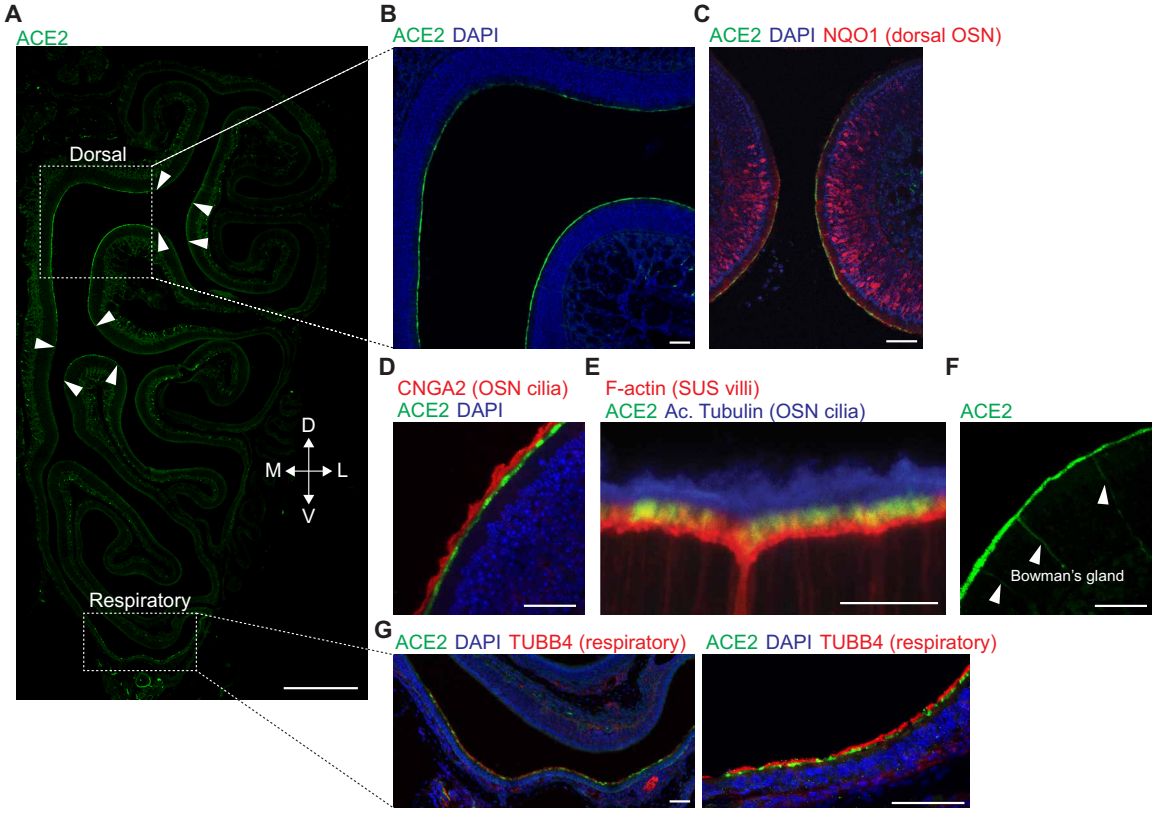

Fig. 5. ACE2 protein is detected in the mouse OE and RE. (**A**) ACE2 immunostaining of mouse main OE. As shown in this coronal section, ACE2 protein is detected in the dorsal zone and RE. The punctate Ace2 staining beneath the epithelial layer is likely associated with vasculature. Scale bar, 500 μm. Arrowheads depict the edges of ACE2 expression, corresponding to the presumptive dorsal zone [confirmed in (C)]. Dashed boxes indicate the areas shown in (B) and (G) (left). D, dorsal; L, lateral; M, medial; V, ventral. (**B**) ACE2 protein is detected in the dorsal zone of the OE. Scale bar, 50 μm. (**C**) Dorsal zone–specific expression of ACE2 in the OE was confirmed by costaining with NQO1, a protein expressed in dorsal zone OSNs. Scale bar, 50 μm. (**D**) ACE2 signal in dorsal OE does not overlap with the cilia of OSNs, as visualized by CNGA2. Scale bar, 50 μm. (**E**) High-magnification image of the apical end of the OE reveals that ACE2 signal is localized at the tip of villi of SUS cells, visualized by phalloidin (F-actin), but does not overlap with cilia of OSNs, as visualized by acetylated tubulin (Ac. Tubulin). Scale bar, 10 μm. (**F**) BGs, which span from the lamina propria to the apical surface (arrowheads), were positive for ACE2 staining. Scale bar, 50 μm. (**G**) ACE2 expression in the RE was confirmed by costaining with TUBB4. Scale bars, 50 μm.

Immunostaining in the OB revealed that blood vessels expressed high levels of ACE2 protein, particularly in pericytes; nearly all pericytes exhibited some degree of staining with ACE2 antibodies. Consistent with the scSeq results, staining was not observed in any neuronal cell type (Fig. 7, F and G). These observations may also hold true for at least some other brain regions, as reanalysis of 10 deeply sequenced scSeq datasets from different regions of the nervous system demonstrated that *Ace2* and *Tmprss2* expression is almost completely absent from neurons, consistent with prior immunostaining results (fig. S10) (*52*, *53*). Given the extensive similarities detailed above in expression patterns for ACE2 and TMPRSS2 in the mouse and human, these findings (from mouse experiments) suggest that OB neurons are likely not a primary site of infection, but that vascular pericytes may be sensitive to CoV-2.

DISCUSSION

Here, we show that subsets of OE SUS cells, HBCs, and BG cells in both mouse and human samples express the CoV-2 receptor ACE2 and the S protein protease TMPRSS2. Human OE SUS cells express these genes at levels comparable to those observed in lung cells. In contrast, we failed to detect ACE2 expression in human or mouse OSNs at either the transcript or protein levels. Similarly, mouse vascular pericytes in the OB express ACE2, while we did not detect ACE2 in OB neurons. Thus, primary infection of non-neuronal cell types—rather than sensory or bulb neurons—may be responsible for anosmia and related disturbances in odor perception in patients with COVID-19.

The identification of non-neuronal cell types in the OE and OB susceptible to CoV-2 infection suggests four possible, non-mutually exclusive mechanisms for the acute loss of smell reported in patients with COVID-19. First, local infection of support and vascular cells in the nose and bulb could cause significant inflammatory responses (including cytokine release) whose downstream effects could block effective odor conduction or alter the function of OSNs or OB neurons (*14*, *54*). Second, damage to support cells (which are responsible for local water and ion balance) could indirectly influence signaling from OSNs to the brain (*55*). Third, damage to SUS cells and BG cells in mouse models can lead to OSN death, which in turn could abrogate smell perception (*56*). Last, vascular damage could lead to hypoperfusion and inflammation leading to changes in OB function.

Although scSeq revealed *ACE2* transcripts in only a subset of OE cells, this low level of observed expression matches or exceeds that observed in respiratory cell types that are infected by CoV-2 in patients with COVID-19 (Fig. 3) (*39*). Critically, immunostaining in

Downloaded from http://advances.sciencemag.org/ on October 30, 2020

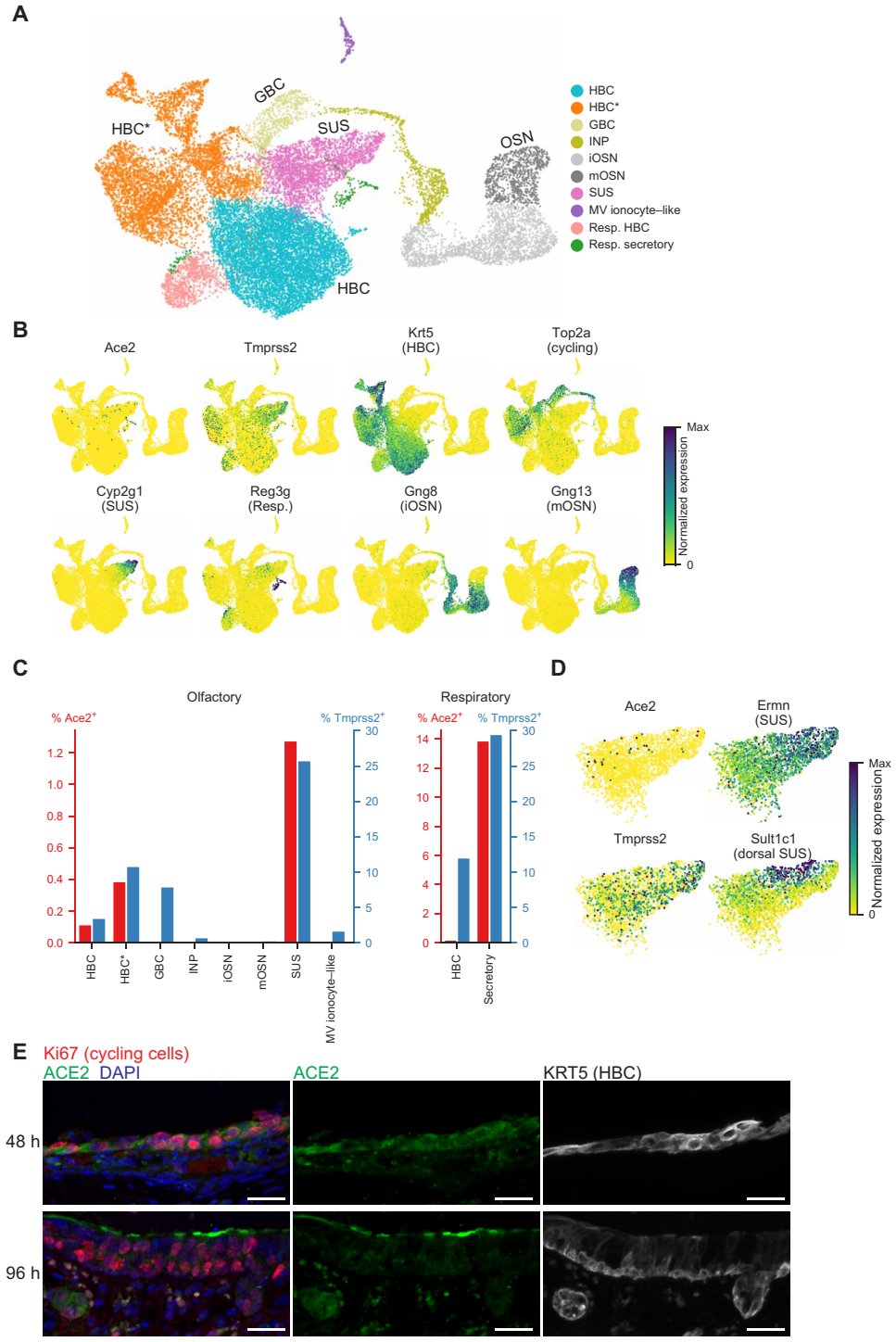

Fig. 6. ACE2 is expressed in the mouse nasal epithelium in an injury model. (**A**) UMAP representation of data from an scSeq HBC lineage dataset, which includes several time points after epithelial injury induced by methimazole. HBC*, activated or cycling HBCs. (**B**) UMAP representation of CoV-2–related genes *Ace2* and *Tmprss2*, as well as marker genes for the HBC-derived cell types. The color represents normalized expression (number of UMIs for a given gene divided by the total number of UMIs for each cell). (**C**) Percentage of cells expressing *Ace2* and *Tmprss2*. *Ace2* is detected in SUS cells, HBCs, activated/cycling HBCs, and respiratory cells. (**D**) UMAP representation of all SUS cells, indicating the normalized expression of CoV-2–related genes *Ace2* and *Tmprss2*, as well as SUS (*Ermn*) cell markers. *Ace2*$^+$ SUS cells are largely a subset of dorsal SUS cells, as identified via the expression of *Sult1c1*. *Sult1c1*$^+$ SUS cells have higher levels of Ace2 ($P = 1.87 \times 10^{-3}$, Mann-Whitney test), and *Ace2*$^+$ SUS cells have higher levels of *Sult1c1* ($P = 8.06 \times 10^{-7}$, Mann-Whitney test). (**E**) ACE2 immunostaining of mouse nasal epithelium after methimazole treatment, together with cycling cell marker Ki67 and HBC marker KRT5. Top: At 48 hours after treatment, ACE2 signal is detected in Ki67$^+$/KRT5$^+$-activated HBCs. Bottom: At 96 hours after treatment, ACE2 signal is observed at the apical surface of Ki67$^+$ cells. Some ACE2$^+$ cells express low levels of the HBC marker KRT5 and have immunostaining patterns similar to that of dorsal SUS cells, suggesting that they are SUS cells in the process of differentiating from their HBC precursors. Scale bars, 25 μm.

Downloaded from http://advances.sciencemag.org/ on October 30, 2020

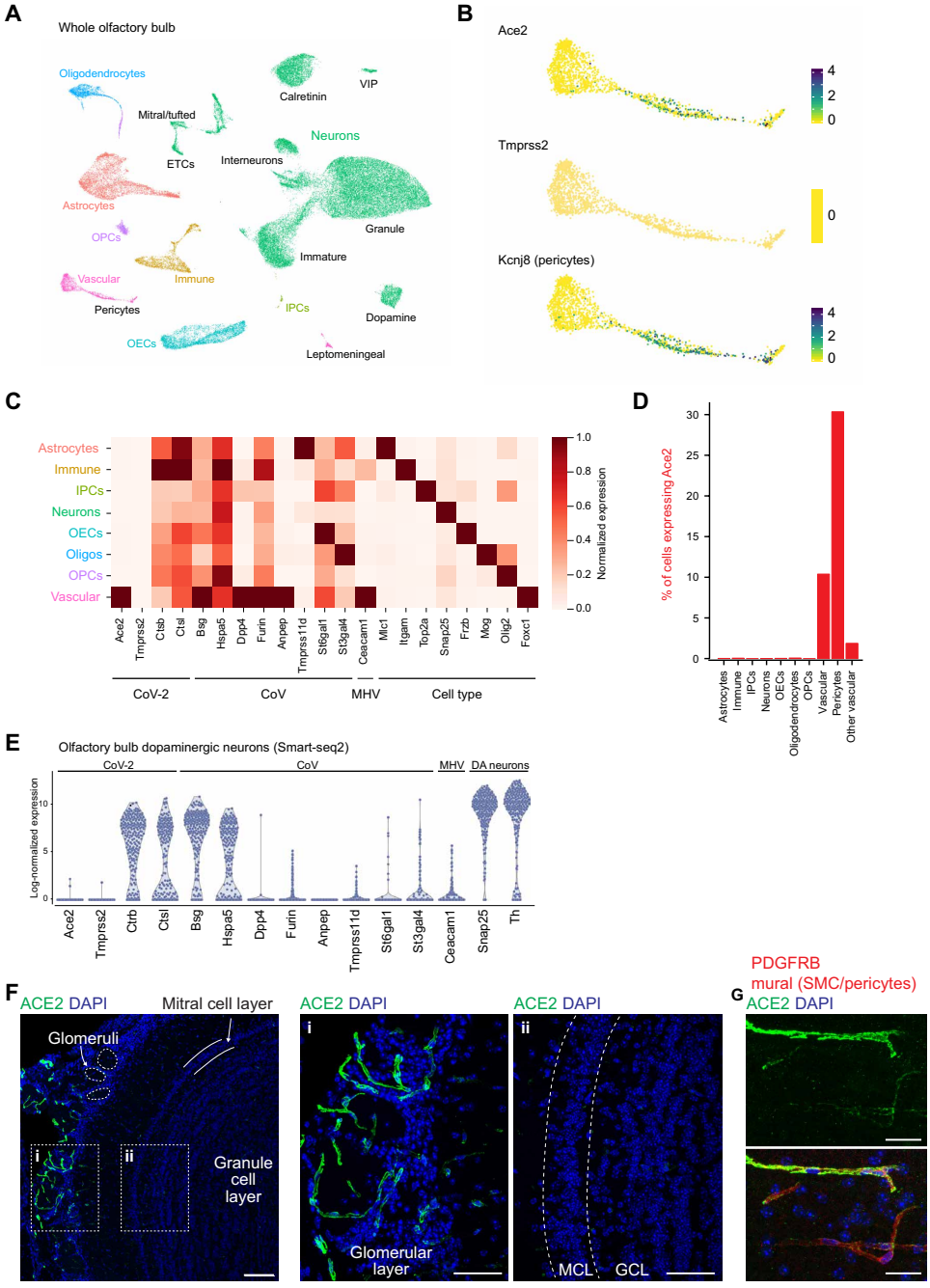

Fig. 7. Expression of coronavirus cell entry–related genes in mouse OB. (**A**) UMAP visualization of OB scSeq highlighting the main cell classes and subtypes from two integrated scSeq datasets (see Materials and Methods). VIP, vasoactive intestinal peptide–expressing neurons; ETCs, external tufted cells; OPCs, oligodendrocyte precursor cells; IPCs, intermediate precursor cells. Cluster information is summarized in figs. S7 and S8. (**B**) UMAP representation of the vascular cell cluster showing expression of CoV-2 entry–related genes (*Ace2* and *Tmprss2*) and *Kcnj8*, a pericyte marker. Color scale depicts log-normalized UMI counts. (**C**) Normalized gene expression of coronavirus cell entry–related genes and cell class markers in mouse OB. Color scale shows scaled mean expression level per cell type, normalized by their maximum expression across cell types. *Ace2* is specifically expressed in vascular cells. (**D**) Percentage of cells expressing *Ace2*. "Other vascular" denotes all vascular cells excluding pericytes. *Ace2* expression was only detected in vascular cell types. (**E**) Log_2-normalized expression [log_2(TPM + 1)] of coronavirus entry genes and dopaminergic neuron markers in manually sorted and deeply sequenced single OB dopaminergic neurons. (**F**) ACE2 immunostaining of the mouse main OB. Left: Section of OB containing the glomerular layer (with example glomeruli circled), mitral cell layer (MCL), and granule cell layer (GCL). ACE2 protein is present in vascular mural cells but not in OB neurons or OSN axons. Boxes (i) and (ii) indicate the locations of enlarged images. Scale bar, 100 μm. (i) Middle: Enlarged image of glomerular layer. ACE2 protein staining was restricted to vascular cells. Scale bar, 50 μm. (ii) Right: Enlarged image of MCL (dashed line) and GCL showing the lack of ACE2. Scale bar, 50 μm. (**G**) An OB section showing ACE2 protein is detected in $PDGFRB^+$ mural cells, including smooth muscle cells and pericytes. Top: ACE2 channel alone. Scale bars, 25 μm.

Downloaded from http://advances.sciencemag.org/ on October 30, 2020

the mouse suggests that ACE2 protein is (nearly) ubiquitously expressed in SUS cells in the dorsal OE, despite sparse detection of *Ace2* transcripts using scSeq. Similarly, nearly all vascular pericytes also expressed ACE2 protein, although only a fraction of OB pericytes were positive for *Ace2* transcripts when assessed using scSeq. Although *Ace2* transcripts were more rarely detected than protein, there was a clear concordance at the cell-type level: Expression of *Ace2* mRNA in a particular cell type accurately predicted the presence of ACE2 protein, while *Ace2* transcript–negative cell types (including OSNs) did not express ACE2 protein. These observations are consistent with recent findings in the RE, suggesting that scSeq substantially underestimates the fraction of a given cell type that expresses the *Ace2* transcript, but that "new" Ace2-expressing cell types are not found with more sensitive forms of analysis (*40*). If our findings in the mouse OE translate to the human (a reasonable possibility given the precise match in olfactory cell types that express CoV-2 cell entry genes between the two species), then ACE2 protein is likely to be expressed in a significant subset of human SUS cells. Thus, there may be many olfactory support cells available for CoV-2 infection in the human epithelium, which in turn could nucleate a pathophysiological process that culminates in anosmia. However, it remains possible that damage to the OE could be caused by more limited cell infection. For example, infection of subsets of SUS cells by the coronavirus SDAV (sialodacryoadenitis virus) in rats ultimately leads to disruption of the global architecture of the OE, suggesting that focal coronavirus infection may be sufficient to cause diffuse epithelial damage (*56*).

We observe that activated HBCs, which are recruited after injury, express *Ace2* at higher levels than those apparent in resting stem cells. The natural history of CoV-2–induced anosmia is only now being defined; while recovery of smell on time scales of weeks in many patients has been reported, it remains unclear whether, in a subset of patients, smell disturbances will be long-lasting or permanent (*8*–*12*, *57*). While on its own it is unlikely that infection of stem cells would cause acute smell deficits, the capacity of CoV-2 to infect stem cells may play an important role in those cases in which COVID-19–associated anosmia is persistent, a context in which infection of stem cells could inhibit OE regeneration and repair over time.

Two anosmic patients with COVID-19 have presented with functional magnetic resonance imaging–identified hyperintensity in both OBs that reverted to normal after resolution of the anosmia (*58*, *59*), consistent with central involvement in at least some cases. Many viruses, including coronaviruses, have been shown to propagate from the nasal epithelium past the cribriform plate to infect the OB; this form of central infection has been suggested to mediate olfactory deficits, even in the absence of lasting OE damage (*60*–*65*). The rodent coronavirus MHV (mouse hepatitis virus) passes from the nose to the bulb, although rodent OSNs do not express *Ceacam1*, the main MHV receptor (figs. S4C, S5E, and S6A) (*61*, *66*), suggesting that CoVs in the nasal mucosa can reach the brain through mechanisms independent of axonal transport by sensory nerves; OB dopaminergic juxtaglomerular cells express *Ceacam1* (Fig. 7E), which likely supports the ability of MHV to target the bulb and change odor perception. Although SARS-CoV has been shown to infect the OB in a transgenic mouse model that ectopically expresses human ACE2 (*65*), it is unclear to what extent similar results will be observed for CoV-2 in this mouse and in recently developed mouse models expressing human ACE2 that better recapitulate native expression patterns (*67*–*69*). One speculative possibility is that local seeding of the OE with CoV-2–infected cells can result in OSN-independent transfer of virions from the nose to the bulb, perhaps via the vascular supply shared between the OB and the OSN axons that comprise CN I. Although CN I was not directly queried in our datasets, it is reasonable to infer that vascular pericytes in CN I also express ACE2, which suggests a possible route of entry for CoV-2 from the nose into the brain. Given the absence of ACE2 in mouse OB neurons—and the near-ubiquity of ACE2 expression in OB pericytes—we speculate that any central olfactory dysfunction in COVID-19 is the secondary consequence of inflammation arising locally from pericytes, or in response to diffusable factors arising from more distant sources (*51*).

Multiple immunostaining studies reveal that ACE2 protein in the human brain is predominantly or exclusively expressed in vasculature (and specifically expressed within pericytes) (*52*, *53*, *70*), and many neurological symptoms associated with CoV-2 infection such as stroke or altered consciousness are consistent with an underlying vasculopathy (*71*–*76*). In addition, human cerebrospinal fluid (CSF) samples have failed thus far to reveal CoV-2 RNA (*73*, *77*), and autopsies from human patients have found that the brain contains the lowest levels of CoV-2 across organs sampled (*78*). On the other hand, multiple other studies have suggested that ACE2 may be expressed in human neurons and glia (*79*–*82*). In addition, two recent studies in mouse models expressing human ACE2 have found CoV-2 in the brain after intranasal inoculation (*67*, *68*), although neither specifically queried the OB; this work stands in contrast to results in a nonhuman primate model of COVID-19, in which nasal infection did not lead to the presence of identifiable CoV-2 antigens in the brain (*83*). Further work will be required to resolve these inconsistencies and to definitively characterize the distribution of ACE2 protein and ultimately CoV-2–infected cells in the human OB and brain.

We note several caveats that temper our conclusions. Although current data suggest that ACE2 is the most likely receptor for CoV-2 in vivo, it is possible (although it has not yet been demonstrated) that other molecules such as BSG (basigin) may enable CoV-2 entry independently of ACE2 (figs. S1E, S4C, S5E, and S6A) (*84*, *85*). In addition, it has recently been reported that low-level expression of ACE2 can support CoV-2 cell entry (*86*); it is possible, therefore, that ACE2 expression beneath the level of detection in our assays may yet enable CoV-2 infection of apparently ACE2-negative cell types. We also propose that damage to the olfactory system is due to either primary infection or secondary inflammation; it is possible (although it has not yet been demonstrated) that cells infected with CoV-2 can form syncytia with cells that do not express ACE2. Such a mechanism could damage neurons adjacent to infected cells. Last, it has recently been reported that inflammation can induce expression of ACE2 in human cells (*87*, *88*). It is therefore possible that our survey of ACE2 expression, and other recent reports demonstrating expression of ACE2 in OE support and stem cells but not neurons (*81*, *89*, *90*), might underrepresent the cell types that express ACE2 under conditions of CoV-2 infection.

Any reasonable pathophysiological mechanism for COVID-19–associated anosmia must account for the high penetrance of smell disorders relative to endemic viruses (*12*, *91*, *92*), the apparent suddenness of smell loss that can precede the development of other symptoms (*11*, *13*), and the transient nature of dysfunction in many patients (*11*, *17*, *18*); definitive identification of the disease mechanisms underlying COVID-19–mediated anosmia will require additional research. Nonetheless, our identification of cells in the OE and OB

Downloaded from http://advances.sciencemag.org/ on October 30, 2020

expressing molecules known to be involved in CoV-2 entry illuminates a path forward for future studies.

MATERIALS AND METHODS

Human nasal scSeq dataset

Human scSeq data from Durante *et al.* (*38*) were downloaded from the Gene Expression Omnibus (GEO) at accession GSE139522. 10× Genomics mtx files were filtered to remove any cells with fewer than 500 total counts. Additional preprocessing, including normalizing total counts to the median total counts for each cell and filtering for highly variable genes, was performed using the SPRING gene filtering function "filter_genes" with parameters (90, 3, 10). The resulting data were visualized in SPRING and partitioned using Louvain clustering on the SPRING *k*-nearest neighbor graph. Four clusters were removed for quality control, including two with low total counts (likely background) and two with high mitochondrial counts (likely stressed or dying cells). Putative doublets were also identified using Scrublet and removed (7% of cells). The remaining cells were projected to 40 dimensions using principal components analysis (PCA). PCA batch correction was performed using patient 4 as a reference, as previously described (*93*). The filtered data were then repartitioned using Louvain clustering on the SPRING graph, and each cluster was annotated using known marker genes, as described in (*38*). For example, immature OSNs (iOSNs) and mOSNs were identified via their expression of *GNG8* and *GNG13*, respectively. HBCs were identified via the expression of *KRT5* and *TP63*, and olfactory HBCs were distinguished from respiratory HBCs via the expression of *CXCL14* and *MEG3*. Identification of SUS cells (*CYP2A13* and *CYP2J2*), BG (*SOX9* and *GPX3*), and MV ionocyte–like cells (*ASCL3*, *CFTR*, and *FOXI1*) was also performed using known marker genes. For visualization, the top 40 principal components (PCs) were reduced to two dimensions using UMAP with parameters (n_neighbors = 15, min_dist = 0.4).

The filtered human scSeq dataset contained 33,358 cells. Each of the samples contained cells from both the OE and RE, although the frequency of OSNs and respiratory cells varied across patients, as previously described (*38*). A total of 295 cells expressed *ACE2*, and 4953 cells expressed *TMPRSS2*. Of the 865 identified OSNs, including both immature and mature cells, none of the cells express *ACE2*, and only 2 (0.23%) expressed *TMPRSS2*. In contrast, *ACE2* was reliably detected in at least 2%, and *TMPRSS2* was expressed in close to 50% of multiple respiratory epithelial subtypes. The expression of both known cell-type markers and known CoV-related genes was also examined across respiratory and olfactory epithelial cell types. For these gene sets, the mean expression in each cell type was calculated and normalized by the maximum across cell types.

Mapping scSeq datasets to each other

Data from Deprez *et al.* (*41*) were downloaded from the Human Cell Atlas website [www.genomique.eu/cellbrowser/HCA/; "Single-cell atlas of the airway epithelium (Grch38 human genome)"]. A subset of these data was combined with a subset of the Durante *et al.* data for mapping between cell types. For the Deprez *et al.* data, the subset consisted of samples from the nasal RE that belonged to a cell type with >20 cells, including basal, cycling basal, suprabasal, secretory, mucous multiciliated cells, multiciliated, SMG (submucosal gland) goblet, and ionocyte. We observed two distinct subpopulations of basal cells, with one of the two populations distinguished by expression of *CXCL14*. The cells in this population were manually identified using SPRING and defined for downstream analysis as a separate cell-type annotation called "basal (*CXCL14*$^+$)." For the Durante data, the subset consisted of cells from cell types that had some putative similarity to cells in the Deprez dataset, including olfactory HBC, cycling respiratory HBC, respiratory HBC, early respiratory secretory cells, respiratory secretory cells, SUS cells, BG, and olfactory MV cells.

To establish a cell-type mapping:

1) Data from Durante *et al.* (*38*) and Deprez *et al.* (*41*) were combined, and gene expression values were linearly scaled so that all cells across datasets had the same total counts. PCA was then performed using highly variable genes (n = 1477 genes) and PCA batch correction (*93*) with the Durante *et al.* data as a reference set.

2) Mapping was then performed bidirectionally between the two datasets. Each cell from "dataset 1" "voted" for the five most similar cells in "dataset 2," using distance in PCA space as the measure of similarity. A table T counting votes across cell types was then computed, where for cell type i in dataset 1 and cell type j in dataset 2

T_{ij} = {number of votes cast from cells of type i to cells of type j}

Thus, if dataset 1 has N cells, then T would count $5 \times N$ votes ($\Sigma T_{ij} = 5N$).

3) The table of votes T was z-scored against a null distribution, generated by repeating the procedure above 1000 times with shuffled cell-type labels.

The resulting z scores were similar between the two possible mapping directions (Durante → Deprez versus Deprez → Durante; R = 0.87 Pearson correlation of mapping z scores). The mapping z scores were also highly robust upon varying the number of votes cast per cell (R > 0.98 correlation of mapping z scores upon changing the vote numbers to 1 or 50 as opposed to 5). Only cell-type correspondences with a high z score in both mapping directions (z score > 25) were used for downstream analysis.

To establish a common scale of gene expression between datasets, we restricted our analyses to cell-type correspondences that were supported both by bioinformatic mapping and shared a nominal cell-type designation based on marker genes. These included basal/suprabasal cells = "respiratory HBCs" from Durante *et al.* and "basal" and "suprabasal" cells from Deprez *et al.*; secretory cells = "early respiratory secretory cells" and "respiratory secretory cells" from Durante *et al.* and "secretory" cells from Deprez *et al.*; and multiciliated cells = "respiratory ciliated cells" from Durante *et al.* and "multiciliated" cells from Deprez *et al.*

We next sought a transformation of the Durante *et al.* data so that it would agree with the Deprez *et al.* data within the corresponding cell types identified above. To account for differing normalization strategies applied to each dataset before download (log normalization and rescaling with cell-specific factors for Deprez *et al.* but not for Durante *et al.*), we used the following ansatz for the transformation, where the pseudo-count p is a global latent parameter and the rescaling factors f_i are fit to each gene separately. In the equation below, T denotes the transformation, and e_{ij} represents a gene expression value for cell i and gene j in the Durante data

$$T(e_{ij}) = (\log(e_{ij} + p) - \log(p))/f_j$$

The parameter p was fit by maximizing the correlation of average gene expression across all genes between each of the cell-type correspondences listed above. The rescaling factors f_i were then fitted separately for each gene by taking the quotient of average gene expression

Downloaded from http://advances.sciencemag.org/ on October 30, 2020

between the Deprez *et al.* data and the log-transformed Durante *et al.* data, again across the cell-type correspondences listed above.

Mouse bulk RNA-seq datasets

Normalized gene expression tables were obtained from previous published datasets (Table 1) (*43*, *46*–*48*). For the mouse datasets, the means of the replicates from WOM or OSN were used to calculate $\log_2$ fold changes. For the mouse data from Saraiva *et al.* (*43*, *46*) and the primate datasets, the normalized counts of the genes of interest from individual replicates were plotted.

Mouse WOM Drop-seq experiments

Tissue dissection and single-cell dissociation for nasal epithelium

A new dataset of WOM scSeq was generated from adult male mice (8 to 12 weeks old). All mouse husbandry and experiments were performed following institutional and federal guidelines and approved by Harvard Medical School's Institutional Animal Care and Use Committee (IACUC). Briefly, dissected main OE was cleaned up in 750 µl of EBSS (Earle's balanced salt solution; Worthington), and epithelium tissues were isolated in 750 µl of papain (20 U/ml in EBSS) and 50 µl of deoxyribonuclease I (DNase I) (2000 U/ml). Tissue pieces were transferred to a 5-ml round-bottom tube (BD), and 1.75 ml of papain and 450 µl of DNase I were added. After 1- to 1.5-hour incubation with rocking at 37°C, the suspension was triturated with a 5-ml pipette 15 times and passed through a 40-µm cell strainer (BD), and the strainer was washed with 1 ml of Dulbecco's modified Eagle's medium (DMEM) + 10% fetal bovine serum (FBS) (Invitrogen). The cell suspension was centrifuged at 300*g* for 5 min. Cells were resuspended with 4 ml of DMEM + 10% FBS and centrifuged at 300*g* for 5 min. Cells were suspended with phosphate-buffered saline (PBS) + 0.01% bovine serum albumin (BSA), and concentration was measured by a hemocytometer.

Drop-seq experiments

Drop-seq experiments were performed as previously described (*94*). Microfluidics devices were obtained from FlowJEM, and barcode beads were obtained from ChemGenes. Eight 15-min Drop-seq runs were collected in total, which were obtained from five mice.

Sequencing of Drop-seq samples

Eight replicates of Drop-seq samples were sequenced across five runs on an Illumina NextSeq 500 platform. Paired-end reads from the fastq files were trimmed, aligned, and tagged via the Drop-seq tools (v1.13) pipeline, using STAR (v2.5.4a) with genomic indices from Ensembl Release 93. The digital gene expression matrix was generated for 4000 cells for 0126_2; 5000 cells for 0105, 0126_1, 051916_DS11, 051916_DS12, and 051916_DS22; 5500 cells for 051916_DS21; and 9500 cells for 0106.

Preprocessing of Drop-seq samples

Processing of the WOM Drop-seq samples was performed in Seurat (v2.3.1). Cells with less than 500 UMIs or more than 15,000 unique molecular identifiers (UMIs), or higher than 5% mitochondrial genes, were removed. Potential doublets were removed using Scrublet. Cells were initially preprocessed using the Seurat pipeline. Variable genes "FindVariableGenes" (y.cutoff = 0.6) were scaled [regressing out effects due to number of UMIs (nUMI), the percentage of mitochondrial genes, and replicate ids], and the data were clustered using 50 PCs with the Louvain algorithm (resolution = 0.8). In a fraction of SUS cells, we observed coexpression of markers for SUS cells and other cell types (e.g., OSNs). Reclustering of SUS cells alone separated these presumed doublets from the rest of the SUS cells, and the presumed doublets were removed for the analyses described below.

Processing of Drop-seq samples

The filtered cells from the preprocessing steps were reanalyzed in Python using Scanpy and SPRING. In brief, the raw gene counts in each cell were total counts normalized, and variable genes were identified using the SPRING gene filtering function "filter_genes" with parameters (85, 3, 3); mitochondrial and olfactory receptor genes were excluded from the variable gene lists. The resulting 2083 variable genes were *Z*-scored, and the dimensionality of the data was reduced to 35 via PCA. The *k*-nearest neighbor graph (n_neighbors = 15) of these 35 PCs was clustered using the Leiden algorithm (resolution = 1.2) and was reduced to two dimensions for visualization via the UMAP method (min_dist = 0.42). Clusters were manually annotated on the basis of known marker genes, and those sharing markers (e.g. OSNs) were merged.

The mouse WOM Drop-seq dataset contained 29,585 cells that passed the above filtering. Each of the 16 clusters identified contained cells from all eight replicates in roughly equal proportions. Of the 17,666 mOSNs and the 4674 iOSNs, none of the cells express *Ace2*.

Table 1. Sample information for the bulk RNA-seq data analyzed in this study. Three different mouse bulk RNA-seq datasets were used, each with replicates from WOM or purified OSNs. An additional dataset contained bulk RNA-seq data from humans and nonhuman primates. n.s., not specified; OMP, olfactory marker protein; IRES, internal ribosomal entry site; GFP, green fluorescent protein; WT, wild type; NA, not applicable.

	Source	Species	Reps	Samples per rep	Sex (M/F)	Age	Strain	Geno
Saraiva *et al.* (*46*)	WOM	Mouse	3	1	2/1	P21	OMP-IRES-GFP	GFP/+
	OSN	Mouse	3	14–16	Mixed	P25	OMP-IRES-GFP	GFP/+
Kanageswaran *et al.* (*47*)	WOM	Mouse	4	3	F	4 weeks	C57BL/6J	WT
	OSN	Mouse	2	6–8	Mixed	Adult	OMP-IRES-GFP	GFP/+ or GFP/GFP
Colquitt *et al.* (*48*)	WOM	Mouse	2	n.s.	n.s.	3 weeks	Dnmt3a	WT
	OSN	Mouse	2	n.s.	n.s.	3 weeks	Dnmt3a	WT
Saraiva *et al.* (*43*)	WOM	Human	3	1	3/0	n.s.	NA	
	WOM	Macaque	3	1	n.s.	~4.5 years	NA	
	WOM	Marmoset	3	1	n.s.	~1–10 years	NA	

Downloaded from http://advances.sciencemag.org/ on October 30, 2020

In contrast, in the olfactory epithelial cells, *Ace2* expression was observed in the BG, olfactory HBCs, and dorsal SUS cells.

Immunohistochemistry and in situ hybridization of mouse and human tissue

Mouse OE tissue processing

Mice were euthanized with a lethal dose of xylazine, and nasal epithelium with attached OBs was dissected and fixed in 4% paraformaldehyde (Electron Microscope Sciences, 19202) in PBS overnight at 4°C or for 2 hours at room temperature. Tissues were washed three times in PBS (5 min each) and incubated in 0.45 M EDTA in PBS overnight at 4°C. The following day, tissues were rinsed by PBS, incubated in 30% sucrose in PBS for at least 30 min, transferred to Tissue Freezing Medium (VWR, 15146-025) for at least 45 min, frozen on crushed dry ice, and stored at −80°C until sectioning. Tissue sections (20 μm thick for the OB and 12 μm thick for nasal epithelium) were collected on Superfrost Plus glass slides (VWR, 48311703) and stored at −80°C until immunostaining. For methimazole-treated samples, adult C57BL/6J mice (6 to 12 weeks old; JAX stock no. 000664) were given intraperitoneal injections of 50 μg of methimazole per gram of body weight (Sigma-Aldrich, M8506) and euthanized at 24-, 48-, and 96-hour time points.

Immunostaining for mouse tissue

Sections were permeabilized with 0.1% Triton X-100 in PBS for 20 min and then rinsed three times in PBS. Sections were then incubated for 45 to 60 min in blocking solution that consisted of PBS containing 3% BSA (Jackson ImmunoResearch, 001-000-162) and 3% Donkey Serum (Jackson ImmunoResearch, 017-000-121) at room temperature, followed by overnight incubation at 4°C with primary antibodies diluted in the same blocking solution. Primary antibodies used are as follows: goat anti-ACE2 (Thermo Fisher Scientific, PA5-47488; 1:40), mouse anti-TUBB4 (Sigma-Aldrich, T7941; 1:4000), rabbit anti-KRT5 (Abcam, ab52635; 1:200), goat anti-NQO1 (Abcam, ab2346; 1:200), mouse antiacetylated tubulin (Abcam, ab24610; 1:500), rabbit anti-CNGA2 (Abcam, ab79261; 1:100), and rat anti-CD140b/PDGFRB (Thermo Fisher Scientific, 14-1402-82; 1:100).

On the following day, sections were rinsed once and washed three times for 5 to 10 min in PBS and then incubated for 45 min with secondary antibodies diluted in blocking solution at 1:300 ratios and/or Alexa Fluor 555–conjugated phalloidin (1:400). Secondary antibodies used were as follows: donkey anti-goat immunoglobulin G (IgG) Alexa Fluor 488 (Jackson ImmunoResearch, 705-546-147), donkey anti-goat IgG Alexa 555, (Invitrogen, A21432), donkey anti-rabbit IgG Alexa 555 (Invitrogen, A31572), donkey anti-rabbit IgG Alexa 647 (Jackson ImmunoResearch, 711-605-152), donkey anti-mouse IgG Alexa 555 (Invitrogen, A31570), donkey anti-mouse IgG Alexa 647 (Invitrogen, A31571), and donkey anti-rat IgG Alexa 488 (Invitrogen, A21208).

After secondary antibody incubation, sections were washed twice for 5 to 10 min in PBS, incubated with 300 nM 4′,6-diamidino-2-phenylindole (DAPI) in PBS for 10 min, and then rinsed with PBS. Slides were mounted with glass coverslips using VECTASHIELD Mounting Medium (Vector Laboratories, H-1000) or ProLong Diamond Antifade Mountant (Invitrogen, P36961).

For costaining of ACE2 and NQO1, slides were first stained with ACE2 primary antibody and donkey anti-goat IgG Alexa 488 secondary. After three washes of secondary antibody, tissues were incubated with unconjugated donkey anti-goat IgG Fab fragments (Jackson ImmunoResearch, 705-007-003) at 30 μg/ml diluted in blocking solution for 1 hour at room temperature. Tissues were washed twice with PBS, once in blocking solution, and incubated in blocking solution for 30 to 40 min at room temperature, followed by a second round of staining with the NQO1 primary antibody and donkey anti-goat IgG Alexa 555 secondary antibody.

Confocal images were acquired using a Leica SPE microscope (Harvard Medical School Neurobiology Imaging Facility) with 405-, 488-, 561-, and 635-nm laser lines. Multislice *Z*-stack images were acquired, and their maximal intensity projections are shown. For Fig. 5A, tiled images were acquired and stitched by the Leica LAS X software. Images were processed using Fiji ImageJ software (*95*), and noisy images were median-smoothed using the *Remove Outliers* function built into Fiji.

Fluorescence in situ hybridization for mouse tissue

Sult1c1 RNA was detected by fluorescent RNAscope assay (Advanced Cell Diagnostics, kit 320851) using probe 539921-C2, following the manufacturer's protocol (RNAscope Fluorescent Multiplex Kit User Manual, 320293-UM Date 03142017) for paraformaldehyde-fixed tissue. Before initiating the hybridization protocol, the tissue was pretreated with two successive incubations (first 30 min and then 15 min long) in RNAscope Protease III (Advanced Cell Diagnostics, 322337) at 40°C and then washed in distilled water. At the end of the protocol, the tissue was washed in PBS and subjected to the 2-day immunostaining protocol described above.

Immunostaining of human nasal tissue

Human olfactory mucosa biopsies were obtained via the Institutional Review Board–approved protocol at Duke University School of Medicine, from nasal septum or superior turbinate during endoscopic sinus surgery. Tissue was fixed with 4% paraformaldehyde and cryosectioned at 10 μm, and sections were processed for immunostaining, as previously described (*38*).

Sections from a 28-year-old female nasal septum biopsy were stained for ACE2 (Fig. 2E) using the same goat anti-ACE2 (Thermo Fisher Scientific, PA5-47488; 1:40) and the protocol described above for mouse tissue. The human sections were costained with rabbit anti-keratin 5 (Abcam, ab24647; AB_448212, 1:1000) and were detected with Alexa Fluor 488 donkey anti-goat (Jackson ImmunoResearch, 705-545-147) and Alexa Fluor 594 donkey anti-rabbit (Jackson ImmunoResearch, 711-585-152) secondary antibodies (1:300).

As further validation of ACE2 expression and to confirm the lack of ACE2 expression in human OSNs (fig. S2), sections were stained with a rabbit anti-ACE2 (Abcam, ab15348; RRID:AB_301861, used at 1:100) antibody immunogenized against human ACE2 and a mouse Tuj1 antibody against neuron-specific tubulin (BioLegend, 801201; RRID:AB_2313773). Anti-ACE2 was raised against a C-terminal synthetic peptide for human ACE2 and was validated by the manufacturer to not cross-react with ACE1 for immunohistochemical labeling of ACE2 in fruit bat nasal tissue and in human lower airway. Recombinant human ACE2 abolished labeling with this antibody in a previous study in human tissue, further demonstrating its specificity (*53*). The Tuj1 antibody was validated, as previously described (*38*). Biotinylated secondary antibodies (Vector Laboratories), avidin-biotinylated horseradish peroxidase kit (Vector Laboratories), and fluorescein tyramide signal amplification (PerkinElmer) were applied per the manufacturer's instructions. For dual staining, Tuj1 was visualized using Alexa Fluor 594 goat anti-mouse (Jackson ImmunoResearch, 115-585-146; RRID: AB_2338881).

Human sections were counterstained with DAPI, and coverslips were mounted using ProLong Gold (Invitrogen) for imaging, using

Downloaded from http://advances.sciencemag.org/ on October 30, 2020

a Leica DMi8 microscope system. Images were processed using Fiji ImageJ software (National Institutes of Health). Scale bars were applied directly from the Leica acquisition software metadata in ImageJ tools. Unsharp mask was applied in ImageJ, and brightness/contrast was adjusted globally.

WOM and HBC lineage–tracing mouse 10× scSeq experiments

Mice

Two-month-old and 18-month-old wild-type C57BL/6J mice were obtained from the National Institute on Aging Aged Rodent Colony and used for the WOM experiments; each experimental condition consisted of one male and one female mouse to aid doublet detection. Mice containing the transgenic *Krt5-CreER*(*T2*) driver (*96*) and *Rosa26*–yellow fluorescent protein (*YFP*) reporter allele (*97*) were used for the HBC lineage–tracing dataset. All mice were assumed to be of normal immune status. Animals were maintained and treated according to federal guidelines under IACUC oversight at the University of California, Berkeley.

Single-cell RNA sequencing

The OE was surgically removed, and the dorsal, sensory portion was dissected and dissociated, as previously described (*36*). For WOM experiments, dissociated cells were subjected to fluorescence-activated cell sorting (FACS) using propidium iodide to identify and select against dead or dying cells; 100,000 cells per sample were collected in 10% FBS. For the HBC lineage–tracing experiments, *Krt5-CreER*; *Rosa26YFP*/*YFP* mice were injected once with tamoxifen (0.25 mg of tamoxifen per gram of body weight) at postnatal day 21 (P21) to P23 of age and euthanized at 24 hours, 48 hours, 96 hours, 7 days, and 14 days after injury, as previously described (*36*, *98*). For each experimental time point, YFP^+ cells were isolated by FACS based on YFP expression and negative for propidium iodide, a vital dye.

Cells isolated by FACS were subjected to scSeq. Three replicates (defined here as a FACS collection run) per age were analyzed for the WOM experiment; at least two biological replicates were collected for each experimental condition for the HBC lineage–tracing experiment. Single-cell complementary DNA (cDNA) libraries from the isolated cells were prepared using the Chromium Single Cell 3′ System according to the manufacturer's instructions. The WOM preparation used v3 chemistry with the following modification: The cell suspension was directly added to the reverse transcription master mix, along with the appropriate volume of water to achieve the approximate cell capture target. The HBC lineage–tracing experiments were performed using v2 chemistry. The 0.04% (w/v) BSA washing step was omitted to minimize cell loss. Completed libraries were sequenced on Illumina HiSeq 4000 to produce paired-end 100-nucleotide reads.

Sequence data were processed with the 10× Genomics Cell Ranger pipeline (2.0.0 for v2 chemistry), resulting in the initial starting number before filtering of 60,408 WOM cells and 25,469 HBC lineage–traced cells. The scone R/Bioconductor package (*99*) was used to filter out lowly expressed genes (fewer than two UMIs in fewer than five cells) and low-quality libraries (using the metric_sample_filter function with arguments hard_nreads = 2000, zcut = 4).

Preliminary filtering

Cells with coexpression of male (*Ddx3y*, *Eif2s3y*, *Kdm5d*, and *Uty*) and female marker genes (*Xist*) were removed as potential doublets from the WOM dataset. For both datasets, doublet cell detection was performed per sample using DoubletFinder (*100*) and Scrublet (*101*). Genes with at least three UMIs in at least five cells were used for downstream clustering and cell-type identification. For the HBC lineage–tracing dataset, the Bioconductor package scone was used to pick the top normalization ("none,fq,ruv_k = 1,no_bio,batch"), corresponding to full quantile normalization, batch correction, and removing one factor of unwanted variation using the RUVSeq Bioconductor package (*102*). A range of cluster labels were created by clustering using the partitioning around medoids algorithm and hierarchical clustering in the clusterExperiment Bioconductor package (*103*), with parameters k0s = (10, 13, 16, 19, 22, 25) and alpha = (NA, 0.1, 0.2, 0.3). Clusters that did not show differential expression were merged (using the function mergeClusters with arguments mergeMethod = "adjP," cutoff = 0.01, and DEMethod = "limma" for the lineage-traced dataset). Initial clustering identified one macrophage (*Msr1*$^+$) cluster consisting of 252 cells; upon its removal and restarting from the normalization step, a subsequent set of 15 clusters was obtained. These clusters were used to filter out 1515 cells for which no stable clustering could be found (i.e., "unassigned" cells) and four clusters respectively consisting of 31, 29 and 23 and 305 cells. Doublets were identified using DoubletFinder, and 271 putative doublets were removed. Inspection of the data in a three-dimensional UMAP embedding identified two groups of cells whose experimentally sampled time point did not match their position along the HBC differentiation trajectory, and these additional 219 cells were also removed from subsequent analyses.

Analysis of CoV-related genes in WOM and HBC lineage 10× datasets

Analysis of WOM scSeq data was performed in Python using the open-source Scanpy software starting from the raw UMI count matrix of the 40,179 cells passing the initial filtering and quality control criteria described above. UMIs were total count–normalized and scaled by 10,000 [TPT (tag per ten thousands)] and then log-normalized. For each gene, the residuals from linear regression models using the total number of UMIs per cell as predictors were then scaled via *Z* scoring. PCA was then performed on a set of highly variable genes (excluding olfactory receptor genes) calculated using the "highly_variable_genes" function with the following parameters: min_mean = 0.01, max_mean = 10, and min_disp = 0.5. A batch-corrected neighborhood graph was constructed by the "bbknn" function with 42 PCs with the following parameters: local_connectivity = 1.5 and embedding two dimensions using the UMAP function with default parameters (min_dist = 0.5). Cells were clustered using the neighborhood graph via the Leiden algorithm (resolution = 1.2). Identified clusters were manually merged and annotated on the basis of known marker gene expression. We removed 281 cells containing mixtures of marker genes with no clear gene expression signature. The identified cell types and the number of each of the remaining 39,898 cells detected were as follows: 28,769 mOSNs, 2607 iOSNs, 859 immediate neural precursors (INPs), 623 GBCs, HBCs (1083 olfactory and 626 respiratory), 480 SUS cells, 331 BG, MV cells (563 brush-like and 1530 ionocyte-like), 92 olfactory ensheathing cells (OECs), 76 respiratory secretory cells, 227 respiratory unspecified cells, 172 atypical OSNs, 1757 various immune cells, and 103 red blood cells. TPT gene expression levels were visualized in two-dimensional UMAP plots.

The filtered HBC lineage dataset containing 21,722 cells was analyzing in Python and processed for visualization using pipelines in SPRING and Scanpy (*104*, *105*). In brief, total counts were normalized to the median total counts for each cell, and highly variable genes were selected using the SPRING gene filtering function ("filter_genes") using parameters (90, 3, 3). The dimensionality of the data

Downloaded from http://advances.sciencemag.org/ on October 30, 2020

was reduced to 20 using PCA and visualized in two dimensions using the UMAP method with parameters (n_neighbors = 20, min_dist = 0.5). Clustering was performed using the Leiden algorithm (resolution = 1.45), and clusters were merged manually using known marker genes. The identified cell types and number of each type were 929 mOSNs, 2073 iOSNs, 786 INPs, 755 GBCs, HBCs (7782 olfactory, 5418 regenerating, and 964 respiratory), 2666 SUS cells, and 176 ionocyte-like MV cells.

Expression of candidate CoV-2–related genes was defined if at least one transcript (UMI) was detected in that cell, and the percentage of cells expressing candidate genes was calculated for each cell type. In the WOM dataset, *Ace2* was only detected in 2 of 28,769 mOSNs (0.007%), and in the HBC lineage dataset, *Ace2* was not detected in any OSNs. Furthermore, *Ace2* was not detected in immature sensory neurons (GBCs, INPs, or iOSNs) in either dataset.

Mouse HBC lineage Smart-seq2 dataset

scSeq data from HBC-derived cells from Fletcher *et al.* (*36*) and Gadye *et al.* (*98*), labeled via *Krt5-CreER* driver mice, were downloaded from GEO at accession GSE99251 using the file "GSE95601_oeHBCdiff_Cufflinks_eSet_counts_table.txt.gz". Processing was performed as described above, including total count normalization and filtering for highly variable genes using the SPRING gene filtering function "filter_genes" with parameters (75, 20, 10). The resulting data were visualized in SPRING, and a subset of cells were removed for quality control, including a cluster of cells with low total counts and another with predominantly reads from ERCC (External RNA Controls Consortium) spike-in controls. Putative doublets were also identified using Scrublet and removed (6% of cells) (*101*). The resulting data were visualized in SPRING and partitioned using Louvain clustering on the SPRING *k*-nearest neighbor graph using the top 40 PCs. Cell-type annotation was performed manually using the same set of marker genes listed above. Three clusters were removed for quality control, including one with low total counts, one with predominantly reads from ERCC spike-in controls (likely background), and one with high mitochondrial counts (likely stressed cells). For visualization and clustering, the remaining cells were projected to 15 dimensions using PCA and visualized with UMAP with parameters (n_neighbors = 15, min_dist = 0.4, alpha = 0.5, maxiter = 500). Clustering was performed using the Leiden algorithm (resolution = 0.4), and cell types were manually annotated using known marker genes.

The filtered dataset of mouse HBC-derived cells contained 1450 cells. The percentage of cells expressing each marker gene was calculated as described above. Of the 51 OSNs identified, none of them expressed *Ace2*, and only 1 of 194 INPs and iOSNs expressed *Ace2*. In contrast, *Ace2* and *Tmprss2* were both detected in HBCs and SUS cells.

Juvenile and adult mouse whole OB scSeq dataset

Juvenile mouse data

scSeq data from whole mouse OB (*50*) were downloaded from mousebrain.org/loomfiles_level_L1.html in loom format (l1 olfactory.loom) and converted to a Seurat object. Samples were obtained from juvenile mice (age P26 to P29). This dataset comprises 20,514 cells that passed cell quality filters, excluding 122 cells identified as potential doublets.

Tissue dissection and single-cell dissociation

A new dataset of whole OB scSeq was generated from adult male mice (8 to 12 weeks old). All mouse husbandry and experiments were performed following institutional and federal guidelines and approved by Harvard Medical School's IACUC. Briefly, dissected OBs (including the accessory OB and fractions of the anterior olfactory nucleus) were dissociated in 750 µl of dissociation medium (DM; Hanks' balanced salt solution containing 10 mM Hepes, 1 mM $MgCl_2$, and 33 mM D-glucose) with papain (28 U/ml) and DNase I (386 U/ml; Worthington). Minced tissue pieces were transferred to a 5-ml round-bottom tube (BD). DM was added to a final volume of 3.3 ml, and the tissue was mechanically triturated five times with a P1000 pipette tip. After 1-hour incubation with rocking at 37°C, the suspension was triturated with a 10-ml pipette 10 times, and 2.3 ml was passed through 40-µm cell strainer (BD). The suspension was then mechanically triturated with a P1000 pipette tip 10 times, and 800 µl was filtered on the same strainer. The cell suspension was further triturated with a P200 pipette tip 10 times and filtered. One milliliter of Quench buffer (22 ml of DM, 2.5 ml of protease inhibitor prepared by resuspending one vial of protease inhibitor with 32 ml of DM, and 2000 U of DNase I) was added to the suspension and centrifuged at 300*g* for 5 min. Cells were resuspended with 3 ml of Quench buffer, overlaid gently on top of 5 ml of protease inhibitor, and then spun down at 70*g* for 10 min. The pellet was resuspended using DM supplemented with 0.04% BSA and spun down at 300*g* for 5 min. Cells were suspended in 400 µl of DM with 0.04% BSA.

OB Drop-seq experiments

Drop-seq experiments were performed as previously described (*94*). Microfluidics devices were obtained from FlowJEM, and barcode beads were obtained from ChemGenes. Two 15-min Drop-seq runs were collected from a single dissociation preparation obtained from two mice. Two such dissociations were performed, giving four total replicates.

Sequencing of Drop-seq samples

Four replicates of Drop-seq samples were pooled and sequenced across three runs on an Illumina NextSeq 500 platform. Paired-end reads from the fastq files were trimmed, aligned, and tagged via the Drop-seq tools (1-2.0) pipeline, using STAR (2.4.2a) with genomic indices from Ensembl Release 82. The digital gene expression matrix was generated for 8000 cells per replicate.

Preprocessing of Drop-seq samples

Cells with low numbers of genes (500), low numbers of UMIs (700), or high numbers of UMIs (>10,000) were removed (6% of cells). Potential doublets were identified via Scrublet and removed (3.5% of cells). Overall, this new dataset comprised 27,004 cells.

Integration of whole OB scSeq datasets

Raw UMI counts from juvenile and adult whole OB samples were integrated in Seurat (*106*). Integrating the datasets ensured that clusters with rare cell types could be identified and that corresponding cell types could be accurately matched. As described below (see fig. S7), although some cell types were observed with different frequencies, the integration procedure yielded stable clusters with cells from both datasets. Briefly, raw counts were log-normalized separately, and the 10,000 most variable genes were identified by variance stabilizing transformation for each dataset. The 4529 variable genes present in both datasets, and the first 30 PCs were used as features for identifying the integration anchors. The integrated expression matrix was scaled and dimensionality-reduced using PCA. On the basis of their percentage of explained variance, the first 28 PCs were chosen for UMAP visualization and clustering.

Graph-based clustering was performed using the Louvain algorithm following the standard Seurat workflow. Cluster stability was analyzed

Downloaded from http://advances.sciencemag.org/ on October 30, 2020

with Clustree on a range of resolution values (0.4 to 1.4), with 0.6 yielding the most stable set of clusters (*107*). Overall, 26 clusters were identified, the smallest of which contained only 43 cells with gene expression patterns consistent with blood cells, which were excluded from further visualization plots. Clustering the two datasets separately yielded similar results. Moreover, the distribution of cells from each dataset across clusters was homogeneous (fig. S7), and the clusters corresponded to previous cell class and subtype annotations (*50*). As previously reported, a small cluster of excitatory neurons (cluster 13) contained neurons from the anterior olfactory nucleus. UMAP visualizations of expression level for cell class and cell-type markers, and for genes coding for coronavirus entry proteins, depict log-normalized UMI counts. The heatmap in Fig. 7C shows the mean expression level for each cell class, normalized to the maximum mean value. The percentage of cells per cell class expressing *Ace2* was defined as the percentage of cells with at least one UMI. In cells from both datasets, *Ace2* was enriched in pericytes but was not detected in neurons.

Smart-seq2 sequencing of manually sorted OB dopaminergic neurons

Tissue dissociation and manual cell sorting

Acute OB 300-μm slices were obtained from *Dat-Cre/Flox-tdTomato* [B6.SJL-*Slc6a3*$^{tm1.1(cre)\ Bkmn/J}$, JAX stock 006660/B6.Cg-*Gt*(*ROSA*)*26Sor*$^{tm9(CAG\text{-}tdTomato)Hze}$, JAX stock 007909] P28 mice as previously described (*108*). As part of a wider study, at P27, these mice had undergone brief 24-hour unilateral naris occlusion via a plastic plug insert (n = 5 mice) or were subjected to a sham control manipulation (n = 5 mice); all observed effects here were independent of these treatment groups. Single-cell suspensions were generated using the Neural Tissue Dissociation Kit–Postnatal Neurons (Miltenyi Biotec, catalog no. 130-094-802), following the manufacturer's instructions for manual dissociation, using three fired-polished Pasteur pipettes of progressively smaller diameter. After enzymatic and mechanical dissociations, cells were filtered through a 30-μm cell strainer, centrifuged for 10 min at 4°C, resuspended in 500 μl of artificial cerebrospinal fluid (ACSF) (140 mM NaCl, 1.25 mM KCl, 1.25 mM NaH_2PO_4, 10 mM Hepes, 25 mM glucose, 3 mM $MgCl_2$, and 1 mM $CaCl_2$) with channel blockers [0.1 μM tetrodotoxin (TTX), 20 μM 6-cyano-7-nitroquinoxaline-2,3-dione (CNQX), and 50 μM D-aminophosphovalerate (AP-V)], and kept on ice to minimize excitotoxicity and cell death.

For manual sorting of fluorescently labeled dopaminergic neurons, we adapted a previously described protocol (*109*). Fifty microliters of single-cell suspension was dispersed on 3.5-mm petri dishes (with a Sylgard-covered base) containing 2 ml of ACSF + channel blockers. Dishes were left undisturbed for 15 min to allow the cells to sink and settle. Throughout, dishes were kept on a metal plate on top of ice. tdTomato$^+$ cells were identified by their red fluorescence under a stereoscope. Using a pulled glass capillary pipette attached to a mouthpiece, individual cells were aspirated and transferred to a clean, empty dish containing 2 ml of ACSF + channel blockers. The same cell was then transferred to a third clean plate, changing pipettes for every plate change. Last, each individual cell was transferred to a 0.2-ml polymerase chain reaction (PCR) tube containing 2 μl of lysis buffer (RLT Plus, QIAGEN). The tube was immediately placed on a metal plate sitting on top of dry ice for flash-freezing. Collected cells were stored at −80°C until further processing. Positive (more than 10 cells) and negative (sample collection procedure without picking a cell) controls were collected for each sorting session. In total, we collected samples from 10 mice, averaging 50 tdTomato$^+$ cells collected per session. Overall, less than 2.5 hours elapsed between mouse sacrifice and collection of the last cell in any session.

Preparation and amplification of full-length cDNA and sequencing libraries

Samples were processed using a modified version of the Smart-seq2 protocol (*110*). Briefly, 1 μl of a 1:2,000,000 dilution of ERCC spike-ins (Invitrogen, catalog no. 4456740) was added to each sample, and mRNA was captured using modified oligo (dT) biotinylated beads (Dynabeads, Invitrogen). PCR amplification was performed for 22 cycles. Amplified cDNA was cleaned with a 0.8:1 ratio of Ampure-XP beads (Beckman Coulter). cDNAs were quantified on Qubit using HS DNA reagents (Invitrogen), and selected samples were run on a Bioanalyzer HS DNA chip (Agilent) to evaluate size distribution.

To generate the sequencing libraries, individual cDNA samples were normalized to 0.2 ng/μl, and 1 μl was used for one-quarter standard-sized Nextera XT (Illumina) tagmentation reactions, with 12 amplification cycles. Sample indexing was performed using index sets A and D (Illumina). At this point, individual samples were pooled according to their index set. Pooled libraries were cleaned using a 0.6:1 ratio of Ampure beads and quantified on Qubit using HS DNA reagents and with the KAPA Library Quantification Kits for Illumina (Roche). Samples were sequenced on two separate rapid runs on HiSeq 2500 (Illumina), generating 100–base pair paired-end reads. An additional five samples were sequenced on MiSeq (Illumina).

Full-length cDNA sequencing data processing and analysis

Paired-end read fastq files were demultiplexed, quality-controlled using FastQC (www.bioinformatics.babraham.ac.uk/projects/fastqc/), and trimmed using Trim Galore (www.bioinformatics.babraham.ac.uk/projects/trim_galore/). Reads were pseudo-aligned and quantified using kallisto (*111*) against a reference transcriptome from Ensembl Release 89 (Gencode Release M17 GRCm38.p6) with sequences corresponding to the ERCC spike-ins and the *Cre* recombinase and *tdT* (*tdTomato*) genes added to the index. Transcripts were collapsed into genes using the sumAcrossFeatures function in scater.

Cell-level quality control and cell filtering were performed in scater (*112*). Cells with <1000 genes, <100,000 reads, >75% reads mapping to ERCC spike-ins, >10% reads mapping to mitochondrial genes, or low library complexity were discarded (14% samples). The population of OB cells labeled in *Dat-Cre/Flox-tdTomato* mice is known to include a minor nondopaminergic calretinin$^+$ subgroup (*113*), so calretinin-expressing cells were excluded from all analyses. The scTransform function in Seurat was used to remove technical batch effects.

Expression of CoV-relevant genes in scSeq datasets from various brain regions and sensory systems

An analysis of single-cell gene expression data from 10 studies was performed to investigate the expression of genes coding for coronavirus entry proteins in neurons from a range of brain regions and sensory systems. Processed gene expression data tables were obtained from scSeq studies that evaluated gene expression in retina (GSE81905) (*114*), inner ear sensory epithelium (GSE115934) (*115*, *116*), spiral ganglion (GSE114997) (*117*), ventral midbrain (GSE76381) (*118*), hippocampus (GSE100449) (*119*), cortex (GSE107632) (*120*), hypothalamus (GSE74672) (*121*), visceral motor neurons (GSE78845) (*122*), dorsal root ganglia (GSE59739) (*123*), and spinal cord dorsal horn (GSE103840) (*124*). Smart-seq2 sequencing data from *Vsx2*–green fluorescent protein (GFP)$^+$ cells were used from the retina

Downloaded from http://advances.sciencemag.org/ on October 30, 2020

dataset. A subset of the expression matrix that corresponds to day 0 (i.e., control, undisturbed neurons) was used from the layer VI somatosensory cortex dataset. A subset of the data containing neurons from untreated (control) mice were used from the hypothalamic neuron dataset. From the ventral midbrain dopaminergic neuron dataset, a subset comprising *DAT-Cre/tdTomato*$^+$ neurons from P28 mice was used. A subset comprising type I neurons from wild-type mice was used from the spiral ganglion dataset. The "unclassified" neurons were excluded from the visceral motor neuron dataset. A subset containing neurons that were collected at room temperature was used from the dorsal root ganglia dataset. Expression data from dorsal horn neurons obtained from C57/BL6 wild-type mice and *vGat-Cre-tdTomato* and *vGlut2-eGFP* mouse lines were used from the spinal cord dataset. Inspection of all datasets for batch effects was performed using the scater package (version 1.10.1) (*112*). Publicly available raw count expression matrices were used for the retina, hippocampus, hypothalamus, midbrain, visceral motor neurons, and spinal cord datasets, whereas the normalized expression data were used from the inner ear hair cell datasets. For datasets containing raw counts, normalization was performed for each dataset separately by computing pool-based size factors that are subsequently deconvolved to obtain cell-based size factors using the scran package (version 1.10.2) (*125*). Violin plots were generated in scater.

SUPPLEMENTARY MATERIALS

Supplementary material for this article is available at http://advances.sciencemag.org/cgi/content/full/6/31/eabc5801/DC1

View/request a protocol for this paper from *Bio-protocol*.

REFERENCES AND NOTES

1. W.-J. Guan, Z.-Y. Ni, Y. Hu, W.-H. Liang, C.-Q. Ou, J.-X. He, L. Liu, H. Shan, C.-L. Lei, D. S. C. Hui, B. Du, L.-J. Li, G. Zeng, K.-Y. Yuen, R.-C. Chen, C.-L. Tang, T. Wang, P.-Y. Chen, J. Xiang, S.-Y. Li, J.-L. Wang, Z.-J. Liang, Y.-X. Peng, L. Wei, Y. Liu, Y.-H. Hu, P. Peng, J.-M. Wang, J.-Y. Liu, Z. Chen, G. Li, Z.-J. Zheng, S.-Q. Qiu, J. Luo, C.-J. Ye, S.-Y. Zhu, N.-S. Zhong; China Medical Treatment Expert Group for Covid-19, Clinical characteristics of coronavirus disease 2019 in China. *N. Engl. J. Med.* **382**, 1708–1720 (2020).
2. H. A. Rothan, S. N. Byrareddy, The epidemiology and pathogenesis of coronavirus disease (COVID-19) outbreak. *J. Autoimmun.* **109**, 102433 (2020).
3. Z. Wu, J. M. McGoogan, Characteristics of and important lessons from the coronavirus disease 2019 (COVID-19) outbreak in China. *JAMA* **323**, 1239 (2020).
4. P. Zhou, X.-L. Yang, X.-G. Wang, B. Hu, L. Zhang, W. Zhang, H.-R. Si, Y. Zhu, B. Li, C.-L. Huang, H.-D. Chen, J. Chen, Y. Luo, H. Guo, R.-D. Jiang, M.-Q. Liu, Y. Chen, X.-R. Shen, X. Wang, X.-S. Zheng, K. Zhao, Q.-J. Chen, F. Deng, L.-L. Liu, B. Yan, F.-X. Zhan, Y.-Y. Wang, G.-F. Xiao, Z.-L. Shi, A pneumonia outbreak associated with a new coronavirus of probable bat origin. *Nature* **579**, 270–273 (2020).
5. M. Ceccarelli, M. Berretta, E. Venanzi Rullo, G. Nunnari, B. Cacopardo, Differences and similarities between Severe Acute Respiratory Syndrome (SARS)-CoronaVirus (CoV) and SARS-CoV-2. Would a rose by another name smell as sweet? *Eur. Rev. Med. Pharmacol. Sci.* **24**, 2781–2783 (2020).
6. A. Zumla, J. F. W. Chan, E. I. Azhar, D. S. C. Hui, K.-Y. Yuen, Coronaviruses—Drug discovery and therapeutic options. *Nat. Rev. Drug Discov.* **15**, 327–347 (2016).
7. V. M. Corman, D. Muth, D. Niemeyer, C. Drosten, Hosts and sources of endemic human coronaviruses. *Adv. Virus Res.* **100**, 163–188 (2018).
8. S. H. R. Bagheri, A. M. Asghari, M. Farhadi, A. R. Shamshiri, A. Kabir, S. K. Kamrava, M. Jalessi, A. Mohebbi, R. Alizadeh, A. A. Honarmand, Coincidence of COVID-19 epidemic and olfactory dysfunction outbreak. medRxiv 20041889 [**Preprint**]. 27 March 2020. https://doi.org/10.1101/2020.03.23.20041889.
9. A. Giacomelli, L. Pezzati, F. Conti, D. Bernacchia, M. Siano, L. Oreni, S. Rusconi, C. Gervasoni, A. L. Ridolfo, G. Rizzardini, S. Antinori, M. Galli, Self-reported olfactory and taste disorders in patients with severe acute respiratory coronavirus 2 infection: A cross-sectional study. *Clin. Infect. Dis.* **26**, ciaa330 (2020).
10. R. Wölfel, V. M. Corman, W. Guggemos, M. Seilmaier, S. Zange, M. A. Müller, D. Niemeyer, T. C. Jones, P. Vollmar, C. Rothe, M. Hoelscher, T. Bleicker, S. Brünink, J. Schneider, R. Ehmann, K. Zwirglmaier, C. Drosten, C. Wendtner, Virological assessment of hospitalized patients with COVID-2019. *Nature* **581**, 465–469 (2020).
11. J. R. Lechien, C. M. Chiesa-Estomba, D. R. de Siati, M. Horoi, S. D. le Bon, A. Rodriguez, D. Dequanter, S. Blecic, F. el Afia, L. Distinguin, Y. Chekkoury-Idrissi, S. Hans, I. L. Delgado, C. Calvo-Henriquez, P. Lavigne, C. Falanga, M. R. Barillari, G. Cammaroto, M. Khalife, P. Leich, C. Souchay, C. Rossi, F. Journe, J. Hsieh, M. Edjlali, R. Carlier, L. Ris, A. Lovato, C. de Filippis, F. Coppee, N. Fakhry, T. Ayad, S. Saussez, Olfactory and gustatory dysfunctions as a clinical presentation of mild-to-moderate forms of the coronavirus disease (COVID-19): A multicenter European study. *Eur. Arch. Otorhinolaryngol.* **6**, 1–11 (2020).
12. C. Menni, A. M. Valdes, M. B. Freidin, C. H. Sudre, L. H. Nguyen, D. A. Drew, S. Ganesh, T. Varsavsky, M. J. Cardoso, J. S. El-Sayed Moustafa, A. Visconti, P. Hysi, R. C. E. Bowyer, M. Mangino, M. Falchi, J. Wolf, S. Ourselin, A. T. Chan, C. J. Steves, T. D. Spector, Real-time tracking of self-reported symptoms to predict potential COVID-19. *Nat. Med.* 10.1038/s41591-020-0916-2 (2020).
13. G. Spinato, C. Fabbris, J. Polesel, D. Cazzador, D. Borsetto, C. Hopkins, P. Boscolo-Rizzo, Alterations in smell or taste in mildly symptomatic outpatients with SARS-CoV-2 infection. *JAMA* **323**, 2089 (2020).
14. M. Eliezer, C. Hautefort, A. L. Hamel, B. Verillaud, P. Herman, E. Houdart, C. Eloit, Sudden and complete olfactory loss function as a possible symptom of COVID-19. *JAMA Otolaryngol. Head Neck Surg.* 10.1001/jamaoto.2020.0832 (2020).
15. J. R. Lechien, C. M. Chiesa-Estomba, S. Place, Y. van Laethem, P. Cabaraux, Q. Mat, K. Huet, J. Plzak, M. Horoi, S. Hans, M. Rosaria Barillari, G. Cammaroto, N. Fakhry, D. Martiny, T. Ayad, L. Jouffe, C. Hopkins, S. Saussez; COVID-19 Task Force of YO-IFOS, S. Blecic, D. R. de Siati, P. Leich, C. Souchay, C. Rossi, F. Journe, J. Hsieh, L. Ris, F. el Afia, B. Harmegnies, L. Distinguin, Y. Chekkoury-Idrissi, M. Circiu, P. Lavigne, I. Lopez Delgado, C. Calvo-Henriquez, C. Falanga, F. Coppee, S. D. Bon, A. Rodriguez, D. Dequanter, J.-P. Cornelis, S. Vergez, L. Koenen, M. Giuditta, G. Molteni, M. Tucciarone, T. Radulesco, M. Khalife, A.-F. Fourneau, S. Cherifi, M. Manto, J. Michel, T. Radulesco, G. Molteni, M. Tucciarone, G. Mannelli, G. Cantarella, Clinical and epidemiological characteristics of 1420 european patients with mild-to-moderate coronavirus disease 2019. *J. Intern. Med.* 10.1111/joim.13089 (2020).
16. V. Parma, K. Ohla, M. G. Veldhuizen, M. Y. Niv, C. E. Kelly, A. J. Bakke, K. W. Cooper, C. Bouysset, N. Pirastu, M. Dibattista, R. Kaur, M. T. Liuzza, M. Y. Pepino, V. Schöpf, V. Pereda-Loth, S. B. Olsson, R. C. Gerkin, P. R. Domínguez, J. Albayay, M. C. Farruggia, S. Bhutani, A. W. Fjaeldstad, R. Kumar, A. Menini, M. Bensafi, M. Sandell, I. Konstantinidis, A. D. Pizio, F. Genovese, L. Öztürk, T. Thomas-Danguin, J. Frasnelli, S. Boesveldt, Ö. Saatci, L. R. Saraiva, C. Lin, J. Golebiowski, L.-D. Hwang, M. H. Ozdener, M. D. Guàrdia, C. Laudamiel, M. Ritchie, J. Havlícek, D. Pierron, E. Roura, M. Navarro, A. A. Nolden, J. Lim, K. L. Whitcroft, L. R. Colquitt, C. Ferdenzi, E. V. Brindha, A. Altundag, A. Macchi, A. Nunez-Parra, Z. M. Patel, S. Fiorucci, C. M. Philpott, B. C. Smith, J. N. Lundström, C. Mucignat, J. K. Parker, M. van den Brink, M. Schmuker, F. P. S. Fischmeister, T. Heinbockel, V. D. C. Shields, F. Faraji, E. E. Santamaría, W. E. A. Fredborg, G. Morini, J. K. Olofsson, M. Jalessi, N. Karni, A. D'Errico, R. Alizadeh, R. Pellegrino, P. Meyer, C. Huart, B. Chen, G. M. Soler, M. K. Alwashahi, O. Abdulrahman, A. Welge-Lüssen, P. Dalton, J. Freiherr, C. H. Yan, Jasper H. B. de Groot, V. V. Voznessenskaya, H. Klein, J. Chen, M. Okamoto, E. A. Sell, P. B. Singh, J. Walsh-Messinger, N. S. Archer, S. Koyama, V. Deary, S. Craig Roberts, H. Yanik, S. Albayrak, L. M. Novákov, I. Croijmans, P. P. Mazal, S. T. Moein, E. Margulis, C. Mignot, S. Mariño, D. Georgiev, P. K. Kaushik, B. Malnic, H. Wang, S. Seyed-Allaei, N. Yoluk, S. Razzaghi, J. M. Justice, D. Restrepo, J. W. Hsieh, D. R. Reed, T. Hummel, S. D. Munger, J. E. Hayes, More than smell. COVID-19 is associated with severe impairment of smell, taste, and chemesthesis. medRxiv 20090902 [**Preprint**]. 24 May 2020. https://doi.org/10.1101/2020.05.04.20090902.
17. Y. Lee, P. Min, S. Lee, S.-W. Kim, Prevalence and duration of acute loss of smell or taste in COVID-19 patients. *J. Korean Med. Sci.* **35**, e174 (2020).
18. C. H. Yan, F. Faraji, D. P. Prajapati, C. E. Boone, A. S. DeConde, Association of chemosensory dysfunction and Covid-19 in patients presenting with influenza-like symptoms. *Int. Forum Allergy Rhinol.* 10.1002/alr.22579 (2020).
19. A. Welge-Lussen, M. Wolfensberger, Olfactory disorders following upper respiratory tract infections. *Adv Otorhinolaryngol.* **63**, 125–132 (2006).
20. H. J. Duncan, A. M. Seiden, Long-term follow-up of olfactory loss secondary to head trauma and upper respiratory tract infection. *Arch. Otilaryngol Head Neck Surg.* **121**, 1183–1187 (1995).
21. A. Cavazzana, M. Larsson, M. Münch, A. Hähner, T. Hummel, Postinfectious olfactory loss: A retrospective study on 791 patients. *Laryngoscope* **128**, 10–15 (2018).
22. M. Hoffmann, H. Kleine-Weber, S. Schroeder, N. Krüger, T. Herrler, S. Erichsen, T. S. Schiergens, G. Herrler, N. H. Wu, A. Nitsche, M. A. Müller, C. Drosten, S. Pöhlmann, SARS-CoV-2 cell entry depends on ACE2 and TMPRSS2 and is blocked by a clinically proven protease inhibitor. *Cell* **181**, 271–280.e8 (2020).
23. W. Li, M. J. Moore, N. Vasilieva, J. Sui, S. K. Wong, M. A. Berne, M. Somasundaran, J. L. Sullivan, K. Luzuriaga, T. C. Greenough, H. Choe, M. Farzan, Angiotensin-converting enzyme 2 is a functional receptor for the SARS coronavirus. *Nature* **426**, 450–454 (2003).
24. W. Li, T. C. Greenough, M. J. Moore, N. Vasilieva, M. Somasundaran, J. L. Sullivan, M. Farzan, H. Choe, Efficient replication of severe acute respiratory syndrome coronavirus

Downloaded from http://advances.sciencemag.org/ on October 30, 2020

in mouse cells is limited by murine angiotensin-converting enzyme 2. *J. Virol.* **78**, 11429–11433 (2004).
25. K. Kuba, Y. Imai, S. Rao, H. Gao, F. Guo, B. Guan, Y. Huan, P. Yang, Y. Zhang, W. Deng, L. Bao, B. Zhang, G. Liu, Z. Wang, M. Chappell, Y. Liu, D. Zheng, A. Leibbrandt, T. Wada, A. S. Slutsky, D. Liu, C. Qin, C. Jiang, J. M. Penninger, A crucial role of angiotensin converting enzyme 2 (ACE2) in SARS coronavirus-induced lung injury. *Nat. Med.* **11**, 875–879 (2005).
26. S. Bertram, I. Glowacka, M. A. Muller, H. Lavender, K. Gnirss, I. Nehlmeier, D. Niemeyer, Y. He, G. Simmons, C. Drosten, E. J. Soilleux, O. Jahn, I. Steffen, S. Pohlmann, Cleavage and activation of the severe acute respiratory syndrome coronavirus spike protein by human airway trypsin-like protease. *J. Virol.* **85**, 13363–13372 (2011).
27. S. Bertram, A. Heurich, H. Lavender, S. Gierer, S. Danisch, P. Perin, J. M. Lucas, P. S. Nelson, S. Pöhlmann, E. J. Soilleux, Influenza and SARS-coronavirus activating proteases TMPRSS2 and HAT are expressed at multiple sites in human respiratory and gastrointestinal tracts. *PLOS ONE* **7**, e35876 (2012).
28. H. Chu, C.-M. Chan, X. Zhang, Y. Wang, S. Yuan, J. Zhou, R. K.-H. Au-Yeung, K.-H. Sze, D. Yang, H. Shuai, Y. Hou, C. Li, X. Zhao, V. K.-M. Poon, S. P. Leung, M.-L. Yeung, J. Yan, G. Lu, D.-Y. Jin, G. F. Gao, J. F.-W. Chan, K.-Y. Yuen, Middle East respiratory syndrome coronavirus and bat coronavirus HKU9 both can utilize GRP78 for attachment onto host cells. *J. Biol. Chem.* **293**, 11709–11726 (2018).
29. H. J. Hedrich, *The Laboratory Mouse* (Academic Press, 2012), 845 pp.
30. G. K. Reznik, Comparative anatomy, physiology, and function of the upper respiratory tract. *Environ. Health Perspect.* **85**, 171–176 (1990).
31. Y. Suzuki, J. Schafer, A. I. Farbman, Phagocytic cells in the rat olfactory epithelium after bulbectomy. *Exp. Neurol.* **136**, 225–233 (1995).
32. Y. Suzuki, M. Takeda, A. I. Farbman, Supporting cells as phagocytes in the olfactory epithelium after bulbectomy. *J. Comp. Neurol.* **376**, 509–517 (1996).
33. F. Vogalis, C. C. Hegg, M. T. Lucero, Ionic conductances in sustentacular cells of the mouse olfactory epithelium. *J. Physiol.* **562**, 785–799 (2005).
34. S. Pfister, T. Weber, W. Härtig, C. Schwerdel, R. Elsaesser, I. Knuesel, J.-M. Fritschy, Novel role of cystic fibrosis transmembrane conductance regulator in maintaining adult mouse olfactory neuronal homeostasis. *J. Comp. Neurol.* **523**, 406–430 (2014).
35. R. Choi, B. J. Goldstein, Olfactory epithelium: Cells, clinical disorders, and insights from an adult stem cell niche. *Laryngoscope Investig. Otolaryngol.* **3**, 35–42 (2018).
36. R. B. Fletcher, D. Das, L. Gadye, K. N. Street, A. Baudhuin, A. Wagner, M. B. Cole, Q. Flores, Y. G. Choi, N. Yosef, E. Purdom, S. Dudoit, D. Risso, J. Ngai, Deconstructing olfactory stem cell trajectories at single-cell resolution. *Cell Stem Cell* **20**, 817–830.e8 (2017).
37. J. E. Schwob, W. Jang, E. H. Holbrook, B. Lin, D. B. Herrick, J. N. Peterson, J. Hewitt Coleman, Stem and progenitor cells of the mammalian olfactory epithelium: Taking poietic license. *J. Comp. Neurol.* **525**, 1034–1054 (2017).
38. M. A. Durante, S. Kurtenbach, Z. B. Sargi, J. W. Harbour, R. Choi, S. Kurtenbach, G. M. Goss, H. Matsunami, B. J. Goldstein, Single-cell analysis of olfactory neurogenesis and differentiation in adult humans. *Nat. Neurosci.* **23**, 323–326 (2020).
39. W. Sungnak, N. Huang, C. Bécavin, M. Berg, R. Queen, M. Litvinukova, C. Talavera-López, H. Maatz, D. Reichart, F. Sampaziotis, K. B. Worlock, M. Yoshida, J. L. Barnes; HCA Lung Biological Network, SARS-CoV-2 entry factors are highly expressed in nasal epithelial cells together with innate immune genes. *Nat. Med.* **26**, 681–687 (2020).
40. Y. J. Hou, K. Okuda, C. E. Edwards, D. R. Martinez, T. Asakura, K. H. Dinnon III, T. Kato, R. E. Lee, B. L. Yount, T. M. Mascenik, G. Chen, K. N. Olivier, A. Ghio, L. V. Tse, S. R. Leist, L. E. Gralinski, A. Schäfer, H. Dang, R. Gilmore, S. Nakano, L. Sun, M. L. Fulcher, A. Livraghi-Butrico, N. I. Nicely, M. Cameron, C. Cameron, D. J. Kelvin, A. de Silva, D. M. Margolis, A. Markmann, L. Bartelt, R. Zumwalt, F. J. Martinez, S. P. Salvatore, A. Borczuk, P. R. Tata, V. Sontake, A. Kimple, I. Jaspers, W. K. O'Neal, S. H. Randell, R. C. Boucher, R. S. Baric, SARS-CoV-2 reverse genetics reveals a variable infection gradient in the respiratory tract. *Cell* **182**, 1–18 (2020).
41. M. Deprez, L.-E. Zaragosi, M. Truchi, S. R. Garcia, M.-J. Arguel, K. Lebrigand, A. Paquet, D. Pee'r, C.-H. Marquette, S. Leroy, P. Barbry, A single-cell atlas of the human healthy airways. bioRxiv 884759 [**Preprint**]. 23 December 2019. https://doi.org/10.1101/2019.12.21.884759.
42. F. A. Vieira Braga, G. Kar, M. Berg, O. A. Carpaij, K. Polanski, L. M. Simon, S. Brouwer, T. Gomes, L. Hesse, J. Jiang, E. S. Fasouli, M. Efremova, R. Vento-Tormo, C. Talavera-López, M. R. Jonker, K. Affleck, S. Palit, P. M. Strzelecka, H. V. Firth, K. T. Mahbubani, A. Cvejic, K. B. Meyer, K. Saeb-Parsy, M. Luinge, C.-A. Brandsma, W. Timens, I. Angelidis, M. Strunz, G. H. Koppelman, A. J. van Oosterhout, H. B. Schiller, F. J. Theis, M. van den Berge, M. C. Nawijn, S. A. Teichmann, A cellular census of human lungs identifies novel cell states in health and in asthma. *Nat. Med.* **25**, 1153–1163 (2019).
43. L. R. Saraiva, F. Riveros-McKay, M. Mezzavilla, E. H. Abou-Moussa, C. J. Arayata, M. Makhlouf, C. Trimmer, X. Ibarra-Soria, M. Khan, L. Van Gerven, M. Jorissen, M. Gibbs, C. O'Flynn, S. McGrane, P. Mombaerts, J. C. Marioni, J. D. Mainland, D. W. Logan, A transcriptomic atlas of mammalian olfactory mucosae reveals an evolutionary influence on food odor detection in humans. *Sci. Adv.* **5**, eaax0396 (2019).
44. W. Sungnak, N. Huang, C. Bécavin, M. Berg, HCA Lung Biological Network, SARS-CoV-2 entry genes are most highly expressed in nasal goblet and ciliated cells within human airways. arXiv:2003.06122 [q-bio.CB] (13 March 2020).
45. N. Zhu, D. Zhang, W. Wang, X. Li, B. Yang, J. Song, X. Zhao, B. Huang, W. Shi, R. Lu, P. Niu, F. Zhan, X. Ma, D. Wang, W. Xu, G. Wu, G. F. Gao, W. Tan; China Novel Coronavirus Investigating and Research Team, A novel coronavirus from patients with pneumonia in China, 2019. *N. Engl. J. Med.* **382**, 727–733 (2020).
46. L. R. Saraiva, X. Ibarra-Soria, M. Khan, M. Omura, A. Scialdone, P. Mombaerts, J. C. Marioni, D. W. Logan, Hierarchical deconstruction of mouse olfactory sensory neurons: From whole mucosa to single-cell RNA-seq. *Sci. Rep.* **5**, 18178 (2015).
47. N. Kanageswaran, M. Demond, M. Nagel, B. S. P. Schreiner, S. Baumgart, P. Scholz, J. Altmüller, C. Becker, J. F. Doerner, H. Conrad, S. Oberland, C. H. Wetzel, E. M. Neuhaus, H. Hatt, G. Gisselmann, Deep sequencing of the murine olfactory receptor neuron transcriptome. *PLOS ONE* **10**, e0113170 (2015).
48. B. M. Colquitt, E. Markenscoff-Papadimitriou, R. Duffié, S. Lomvardas, Dnmt3a regulates global gene expression in olfactory sensory neurons and enables odorant-induced transcription. *Neuron* **83**, 823–838 (2014).
49. Z. M. Soler, Z. M. Patel, J. H. Turner, E. H. Holbrook, A primer on viral-associated olfactory loss in the era of COVID-19. *Int. Forum Allergy Rhinol.*, 1–11 (2020).
50. A. Zeisel, H. Hochgerner, P. Lönnerberg, A. Johnsson, F. Memic, J. van der Zwan, M. Häring, E. Braun, L. E. Borm, G. L. Manno, S. Codeluppi, A. Furlan, K. Lee, N. Skene, K. D. Harris, J. Hjerling-Leffler, E. Arenas, P. Ernfors, U. Marklund, S. Linnarsson, Molecular architecture of the mouse nervous system. *Cell* **174**, 999–1014.e22 (2018).
51. L. S. Brown, C. G. Foster, J.-M. Courtney, N. E. King, D. W. Howells, B. A. Sutherland, Pericytes and neurovascular function in the healthy and diseased brain. *Front. Cell. Neurosci.* **13**, 282 (2019).
52. I. Hamming, W. Timens, M. L. C. Bulthuis, A. T. Lely, G. Navis, H. van Goor, Tissue distribution of ACE2 protein, the functional receptor for SARS coronavirus. A first step in understanding SARS pathogenesis. *J. Pathol.* **203**, 631–637 (2004).
53. P. G. Kehoe, S. Wong, N. Al Mulhim, L. E. Palmer, J. S. Miners, Angiotensin-converting enzyme 2 is reduced in Alzheimer's disease in association with increasing amyloid-β and tau pathology. *Alzheimers Res Ther* **8**, 50 (2016).
54. M. Chen, R. R. Reed, A. P. Lane, Chronic inflammation directs an olfactory stem cell functional switch from neuroregeneration to immune defense. *Cell Stem Cell* **25**, 501–513.e5 (2019).
55. L. W. Plasschaert, R. Žilionis, R. Choo-Wing, V. Savova, J. Knehr, G. Roma, A. M. Klein, A. B. Jaffe, A single-cell atlas of the airway epithelium reveals the CFTR-rich pulmonary ionocyte. *Nature* **560**, 377–381 (2018).
56. C. G. D. Bihun, D. H. Percy, Morphologic changes in the nasal cavity associated with sialodacryoadenitis virus infection in the Wistar rat. *Vet. Pathol.* **32**, 1–10 (1995).
57. C. Hopkins, P. Surda, E. Whitehead, B. N. Kumar, Early recovery following new onset anosmia during the COVID-19 pandemic—An observational cohort study. *J. Otolaryngol. Head Neck Surg.* **49**, 26 (2020).
58. L. S. Politi, E. Salsano, M. Grimaldi, Magnetic resonance imaging alteration of the brain in a patient with coronavirus disease 2019 (COVID-19) and anosmia. *JAMA Neurol.*, 10.1001/jamaneurol.2020.2125 (2020).
59. T. Laurendon, T. Radulesco, J. Mugnier, M. Gérault, C. Chagnaud, A.-A. El Ahmadi, A. Varoquaux, Bilateral transient olfactory bulbs edema during COVID-19-related anosmia. *Neurology*, 10.1212/WNL.0000000000009850 (2020).
60. K. Bohmwald, N. M. S. Gálvez, M. Ríos, A. M. Kalergis, Neurologic alterations due to respiratory virus infections. *Front. Cell. Neurosci.* **12**, 386 (2018).
61. S. L. Youngentob, J. E. Schwob, S. Saha, G. Manglapus, B. Jubelt, Functional consequences following infection of the olfactory system by intranasal infusion of the olfactory bulb line variant (OBLV) of mouse hepatitis strain JHM. *Chem. Senses* **26**, 953–963 (2001).
62. R. L. Doty, Systemic diseases and disorders. *Handb. Clin. Neurol.* **164**, 361–387 (2019).
63. E. M. Barnett, S. Perlman, The olfactory nerve and not the trigeminal nerve is the major site of CNS entry for mouse hepatitis virus, strain JHM. *Virology* **194**, 185–191 (1993).
64. J. E. Schwob, S. Saha, S. L. Youngentob, B. Jubelt, Intranasal inoculation with the olfactory bulb line variant of mouse hepatitis virus causes extensive destruction of the olfactory bulb and accelerated turnover of neurons in the olfactory epithelium of mice. *Chem. Senses* **26**, 937–952 (2001).
65. J. Netland, D. K. Meyerholz, S. Moore, M. Cassell, S. Perlman, Severe acute respiratory syndrome coronavirus infection causes neuronal death in the absence of encephalitis in mice transgenic for human ACE2. *J. Virol.* **82**, 7264–7275 (2008).
66. E. Hemmila, C. Turbide, M. Olson, S. Jothy, K. V. Holmes, N. Beauchemin, Ceacam1a$^{-/-}$ mice are completely resistant to infection by murine coronavirus mouse hepatitis virus A59. *J. Virol.* **78**, 10156–10165 (2004).
67. R.-D. Jiang, M.-Q. Liu, Y. Chen, C. Shan, Y.-W. Zhou, X.-R. Shen, Q. Li, L. Zhang, Y. Zhu, H.-R. Si, Q. Wang, J. Min, X. Wang, W. Zhang, B. Li, H.-J. Zhang, R. S. Baric, P. Zhou, X.-L. Yang, Z.-L. Shi, Pathogenesis of SARS-CoV-2 in transgenic mice expressing human angiotensin-converting enzyme 2. *Cell* **182**, 1–9 (2020).

Downloaded from http://advances.sciencemag.org/ on October 30, 2020

68. S.-H. Sun, Q. Chen, H.-J. Gu, G. Yang, Y.-X. Wang, X.-Y. Huang, S.-S. Liu, N.-N. Zhang, X.-F. Li, R. Xiong, Y. Guo, Y.-Q. Deng, W.-J. Huang, Q. Liu, Q.-M. Liu, Y.-L. Shen, Y. Zhou, X. Yang, T.-Y. Zhao, C.-F. Fan, Y.-S. Zhou, C.-F. Qin, Y. C. Wang, A mouse model of SARS-CoV-2 infection and pathogenesis. *Cell Host Microbe*, 10.1016/j.chom.2020.05.020 (2020).
69. L. Bao, W. Deng, B. Huang, H. Gao, J. Liu, L. Ren, Q. Wei, P. Yu, Y. Xu, F. Qi, Y. Qu, F. Li, Q. Lv, W. Wang, J. Xue, S. Gong, M. Liu, G. Wang, S. Wang, Z. Song, L. Zhao, P. Liu, L. Zhao, F. Ye, H. Wang, W. Zhou, N. Zhu, W. Zhen, H. Yu, X. Zhang, L. Guo, L. Chen, C. Wang, Y. Wang, X. Wang, Y. Xiao, Q. Sun, H. Liu, F. Zhu, C. Ma, L. Yan, M. Yang, J. Han, W. Xu, W. Tan, X. Peng, Q. Jin, G. Wu, C. Qin, The pathogenicity of SARS-CoV-2 in hACE2 transgenic mice. *Nature*, 10.1038/s41586-020-2312-y (2020).
70. L. He, M. A. Mäe, Y. Sun, L. Muhl, K. Nahar, E. V. Liébanas, M. J. Fagerlund, A. Oldner, J. Liu, G. Genové, R. Pietilä, L. Zhang, Y. Xie, S. Leptidis, G. Mocci, S. Stritt, A. Osman, A. Anisimov, K. A. Hemanthakumar, M. Räsenen, J. Björkegren, M. Vanlandewijck, K. Blomgren, E. Hansson, T. Mäkinen, X.-R. Peng, T. D. Arnold, K. Alitalo, L. I. Eriksson, U. Lendahl, C. Betsholtz, Pericyte-specific vascular expression of SARS-CoV-2 r eceptor ACE2—Implications for microvascular inflammation and hypercoagulopathy in COVID-19 patients. bioRxiv 088500 [**Preprint**]. 12 May 2020. https://doi.org/10.1101/2020.05.11.088500.
71. Y. Zhang, M. Xiao, S. Zhang, P. Xia, W. Cao, W. Jiang, H. Chen, X. Ding, H. Zhao, H. Zhang, C. Wang, J. Zhao, X. Sun, R. Tian, W. Wu, D. Wu, J. Ma, Y. Chen, D. Zhang, J. Xie, X. Yan, X. Zhou, Z. Liu, J. Wang, B. du, Y. Qin, P. Gao, X. Qin, Y. Xu, W. Zhang, T. Li, F. Zhang, Y. Zhao, Y. Li, S. Zhang, Coagulopathy and antiphospholipid antibodies in patients with Covid-19. *N. Engl. J. Med.* **382**, e38 (2020).
72. N. Poyiadji, G. Shahin, D. Noujaim, M. Stone, S. Patel, B. Griffith, COVID-19–associated acute hemorrhagic necrotizing encephalopathy: CT and MRI features. *Radiology*, 201187 (2020).
73. J. Helms, S. Kremer, H. Merdji, R. Clere-Jehl, M. Schenck, C. Kummerlen, O. Collange, C. Boulay, S. Fafi-Kremer, M. Ohana, M. Anheim, F. Meziani, Neurologic features in severe SARS-CoV-2 infection. *N. Engl. J. Med.* **382**, 2268–2270 (2020).
74. T. Coolen, V. Lolli, N. Sadeghi, A. Rovai, N. Trotta, F. S. Taccone, J. Creteur, S. Henrard, J.-C. Goffard, O. Dewitte, G. Naeije, S. Goldman, X. De Tiege, Early postmortem brain MRI findings in COVID-19 non-survivors. medRxiv 20090316 [**Preprint**]. 8 May 2020. https://doi.org/10.1101/2020.05.04.20090316.
75. T. Chen, D. Wu, H. Chen, W. Yan, D. Yang, G. Chen, K. Ma, D. Xu, H. Yu, H. Wang, T. Wang, W. Guo, J. Chen, C. Ding, X. Zhang, J. Huang, M. Han, S. Li, X. Luo, J. Zhao, Q. Ning, Clinical characteristics of 113 deceased patients with coronavirus disease 2019: Retrospective study. *BMJ* **368**, m1295 (2020).
76. R. Beyrouti, M. E. Adams, L. Benjamin, H. Cohen, S. F. Farmer, Y. Y. Goh, F. Humphries, H. R. Jäger, N. A. Losseff, R. J. Perry, S. Shah, R. J. Simister, D. Turner, A. Chandratheva, D. J. Werring, Characteristics of ischaemic stroke associated with COVID-19. *J. Neurol. Neurosurg. Psychiatry*, jnnp-2020-323586 (2020).
77. T. Schaller, K. Hirschbühl, K. Burkhardt, G. Braun, M. Trepel, B. Märkl, R. Claus, Postmortem examination of patients with COVID-19. *JAMA* **323**, 2518–2520 (2020).
78. V. G. Puelles, M. Lütgehetmann, M. T. Lindenmeyer, J. P. Sperhake, M. N. Wong, L. Allweiss, S. Chilla, A. Heinemann, N. Wanner, S. Liu, F. Braun, S. Lu, S. Pfefferle, A. S. Schröder, C. Edler, O. Gross, M. Glatzel, D. Wichmann, T. Wiech, S. Kluge, K. Pueschel, M. Aepfelbacher, T. B. Huber, Multiorgan and renal tropism of SARS-CoV-2. *N. Engl. J. Med.*, 10.1056/NEJMc2011400 (2020).
79. R. Ueha, K. Kondo, R. Kagoya, S. Shichino, S. Ueha, T. Yamasoba, Background mechanisms of olfactory dysfunction in COVID-19: Expression of ACE2, TMPRSS2, and Furin in the nose and olfactory bulb in human and mice. bioRxiv 097352 [**Preprint**]. 15 May 2020. https://doi.org/10.1101/2020.05.15.097352.
80. M. F. Doobay, L. S. Talman, T. D. Obr, X. Tian, R. L. Davisson, E. Lazartigues, Differential expression of neuronal ACE2 in transgenic mice with overexpression of the brain renin-angiotensin system. *Am. J. Physiol. Regul. Integr. Comp. Physiol.* **292**, R373–R381 (2007).
81. K. Bilinska, P. Jakubowska, C. S. Von Bartheld, R. Butowt, Expression of the SARS-CoV-2 entry proteins, ACE2 and TMPRSS2, in cells of the olfactory epithelium: Identification of cell types and trends with age. *ACS Chem. Nerosci.* **11**, 1555–1562 (2020).
82. R. Chen, K. Wang, J. Yu, Z. Chen, C. Wen, Z. Xu, The spatial and cell-type distribution of SARS-CoV-2 receptor ACE2 in human and mouse brain. bioRxiv 030650 [**Preprint**]. 9 April 2020. https://doi.org/10.1101/2020.04.07.030650.
83. V. J. Munster, F. Feldmann, B. N. Williamson, N. van Doremalen, L. Pérez-Pérez, J. Schulz, K. Meade-White, A. Okumura, J. Callison, B. Brumbaugh, V. A. Avanzato, R. Rosenke, P. W. Hanley, G. Saturday, D. Scott, E. R. Fischer, E. de Wit, Respiratory disease in rhesus macaques inoculated with SARS-CoV-2. *Nature*, 10.1038/s41586-020-2324-7 (2020).
84. Z. Chen, L. Mi, J. Xu, J. Yu, X. Wang, J. Jiang, J. Xing, P. Shang, A. Qian, Y. Li, P. X. Shaw, J. Wang, S. Duan, J. Ding, C. Fan, Y. Zhang, Y. Yang, X. Yu, Q. Feng, B. Li, X. Yao, Z. Zhang, L. Li, X. Xue, P. Zhu, Function of HAb18G/CD147 in invasion of host cells by severe acute respiratory syndrome coronavirus. *J. Infect. Dis.* **191**, 755–760 (2005).
85. K. Wang, W. Chen, Y.-S. Zhou, J.-Q. Lian, Z. Zhang, P. Du, L. Gong, Y. Zhang, H.-Y. Cui, J.-J. Geng, B. Wang, X.-X. Sun, C.-F. Wang, X. Yang, P. Lin, Y.-Q. Deng, D. Wei, X.-M. Yang, Y.-M. Zhu, K. Zhang, Z.-H. Zheng, J.-L. Miao, T. Guo, Y. Shi, J. Zhang, L. Fu, Q.-Y. Wang, H. Bian, P. Zhu, Z.-N. Chen, SARS-CoV-2 invades host cells via a novel route: CD147-spike protein. bioRxiv 988345 [**Preprint**]. 14 March 2020. https://doi.org/10.1101/2020.03.14.988345.
86. M. M. Lamers, J. Beumer, J. van der Vaart, K. Knoops, J. Puschhof, T. I. Breugem, R. B. G. Ravelli, J. Paul van Schayck, A. Z. Mykytyn, H. Q. Duimel, E. van Donselaar, S. Riesebosch, H. J. H. Kuijpers, D. Schippers, W. J. van de Wetering, M. de Graaf, M. Koopmans, E. Cuppen, P. J. Peters, B. L. Haagmans, H. Clevers, SARS-CoV-2 productively infects human gut enterocytes. *Science*, eabc1669 (2020).
87. C. G. K. Ziegler, S. J. Allon, S. K. Nyquist, I. M. Mbano, V. N. Miao, C. N. Tzouanas, Y. Cao, A. S. Yousif, J. Bals, B. M. Hauser, J. Feldman, C. Muus, M. H. Wadsworth II, S. W. Kazer, T. K. Hughes, B. Doran, G. J. Gatter, M. Vukovic, F. Taliaferro, B. E. Mead, Z. Guo, J. P. Wang, D. Gras, M. Plaisant, M. Ansari, I. Angelidis, H. Adler, J. M. S. Sucre, C. J. Taylor, B. Lin, A. Waghray, V. Mitsialis, D. F. Dwyer, K. M. Buchheit, J. A. Boyce, N. A. Barrett, T. M. Laidlaw, S. L. Carroll, L. Colonna, V. Tkachev, C. W. Peterson, A. Yu, H. B. Zheng, H. P. Gideon, C. G. Winchell, P. L. Lin, C. D. Bingle, S. B. Snapper, J. A. Kropski, F. J. Theis, H. B. Schiller, L.-E. Zaragosi, P. Barbry, A. Leslie, H.-P. Kiem, J. L. Flynn, S. M. Fortune, B. Berger, R. W. Finberg, L. S. Kean, M. Garber, A. G. Schmidt, D. Lingwood, A. K. Shalek, J. Ordovas-Montanes; HCA Lung Biological Network. Electronic address: lung-network@humancellatlas.org; HCA Lung Biological Network, SARS-CoV-2 receptor ACE2 is an interferon-stimulated gene in human airway epithelial cells and is detected in specific cell subsets across tissues. *Cell* **181**, 1016–1035.e19 (2020).
88. S. P. Sajuthi, P. De Ford, N. D. Jackson, M. T. Montgomery, J. L. Everman, C. L. Rios, E. Pruesse, J. D. Nolin, E. G. Plender, M. E. Wechsler, A. C. Y. Mak, C. Eng, S. Salazar, V. Medina, E. M. Wohlford, S. Huntsman, D. A. Nickerson, S. Germer, M. C. Zody, G. Abecasis, H. M. Kang, K. M. Rice, R. Kumar, S. Oh, J. Rodriguez-Santana, E. G. Burchard, M. A. Seibold, Type 2 and interferon inflammation strongly regulate SARS-CoV-2 related gene expression in the airway epithelium. bioRxiv 034454 [**Preprint**]. 10 April 2020. https://doi.org/10.1101/2020.04.09.034454.
89. L. Fodoulian, J. Tuberosa, D. Rossier, B. N. Landis, A. Carleton, I. Rodriguez, SARS-CoV-2 receptor and entry genes are expressed by sustentacular cells in the human olfactory neuroepithelium. bioRxiv 013268 [**Preprint**]. 2 April 2020. https://doi.org/10.1101/2020.03.31.013268.
90. M. Chen, W. Shen, N. R. Rowan, H. Kulaga, A. Hillel, M. Ramanathan Jr., A. P. Lane, Elevated ACE2 expression in the olfactory neuroepithelium: Implications for anosmia and upper respiratory SARS-CoV-2 entry and replication. bioRxiv 084996 [**Preprint**]. 9 May 2020. https://doi.org/10.1101/2020.05.08.084996.
91. A. Haehner, J. Draf, S. Draeger, K. de With, T. Hummel, Predictive value of sudden olfactory loss in the diagnosis of COVID-19. medRxiv 20081356 [**Preprint**]. 3 May 2020. https://doi.org/10.1101/2020.04.27.20081356.
92. F. Shweta, K. Murugadoss, S. Awasthi, A. J. Venkatakrishnan, A. Puranik, M. Kang, B. W. Pickering, J. C. O'Horo, P. R. Bauer, R. R. Razonable, P. Vergidis, Z. Temesgen, S. Rizza, M. Mahmood, W. R. Wilson, D. Challener, P. Anand, M. Liebers, Z. Doctor, E. Silvert, H. Solomon, T. Wagner, G. J. Gores, A. W. Williams, J. Halamka, V. Soundararajan, A. D. Badley, augmented curation of unstructured clinical notes from a massive EHR system reveals specific phenotypic signature of impending COVID-19 diagnosis. arXiv:2004.09338 [cs.LG] (17 April 2020).
93. C. Weinreb, A. Rodriguez-Fraticelli, F. D. Camargo, A. M. Klein, Lineage tracing on transcriptional landscapes links state to fate during differentiation. *Science* **367**, eaaw3381 (2020).
94. E. Z. Macosko, A. Basu, R. Satija, J. Nemesh, K. Shekhar, M. Goldman, I. Tirosh, A. R. Bialas, N. Kamitaki, E. M. Martersteck, J. J. Trombetta, D. A. Weitz, J. R. Sanes, A. K. Shalek, A. Regev, S. A. McCarroll, Highly parallel genome-wide expression profiling of individual cells using nanoliter droplets. *Cell* **161**, 1202–1214 (2015).
95. J. Schindelin, I. Arganda-Carreras, E. Frise, V. Kaynig, M. Longair, T. Pietzsch, S. Preibisch, C. Rueden, S. Saalfeld, B. Schmid, J.-Y. Tinevez, D. J. White, V. Hartenstein, K. Eliceiri, P. Tomancak, A. Cardona, Fiji: An open-source platform for biological-image analysis. *Nat. Methods* **9**, 676–682 (2012).
96. A. K. Indra, X. Warot, J. Brocard, J.-M. Bornert, J.-H. Xiao, P. Chambon, D. Metzger, Temporally-controlled site-specific mutagenesis in the basal layer of the epidermis: Comparison of the recombinase activity of the tamoxifen-inducible Cre-ER^{T} and Cre-ER^{T2} recombinases. *Nucleic Acids Res.* **27**, 4324–4327 (1999).
97. S. Srinivas, T. Watanabe, C. S. Lin, C. M. William, Y. Tanabe, T. M. Jessell, F. Costantini, Cre reporter strains produced by targeted insertion of EYFP and ECFP into the ROSA26 locus. *BMC Dev. Biol.* **1**, 4 (2001).
98. L. Gadye, D. Das, M. A. Sanchez, K. Street, A. Baudhuin, A. Wagner, M. B. Cole, Y. G. Choi, N. Yosef, E. Purdom, S. Dudoit, D. Risso, J. Ngai, R. B. Fletcher, Injury activates transient olfactory stem cell states with diverse lineage capacities. *Cell Stem Cell* **21**, 775–790.e9 (2017).
99. M. B. Cole, D. Risso, A. Wagner, D. DeTomaso, J. Ngai, E. Purdom, S. Dudoit, N. Yosef, Performance assessment and selection of normalization procedures for single-Cell RNA-seq. *Cell Syst.* **8**, 315–328.e8 (2019).

Downloaded from http://advances.sciencemag.org/ on October 30, 2020

100. C. S. McGinnis, L. M. Murrow, Z. J. Gartner, DoubletFinder: Doublet detection in single-cell RNA sequencing data using artificial nearest neighbors. *Cell Syst.* **8**, 329–337.e4 (2019).
101. S. L. Wolock, R. Lopez, A. M. Klein, Scrublet: Computational identification of cell doublets in single-cell transcriptomic data. *Cell Syst.* **8**, 281–291.e9 (2019).
102. D. Risso, J. Ngai, T. P. Speed, S. Dudoit, Normalization of RNA-seq data using factor analysis of control genes or samples. *Nat. Biotechnol.* **32**, 896–902 (2014).
103. D. Risso, L. Purvis, R. B. Fletcher, D. Das, J. Ngai, S. Dudoit, E. Purdom, clusterExperiment and RSEC: A bioconductor package and framework for clustering of single-cell and other large gene expression datasets. *PLOS Comput. Biol.* **14**, e1006378 (2018).
104. C. Weinreb, S. Wolock, A. M. Klein, SPRING: A kinetic interface for visualizing high dimensional single-cell expression data. *Bioinformatics* **34**, 1246–1248 (2018).
105. F. A. Wolf, P. Angerer, F. J. Theis, SCANPY: Large-scale single-cell gene expression data analysis. *Genome Biol.* **19**, 15 (2018).
106. T. Stuart, A. Butler, P. Hoffman, C. Hafemeister, E. Papalexi, W. M. Mauck III, Y. Hao, M. Stoeckius, P. Smibert, R. Satija, Comprehensive integration of single-cell data. *Cell* **177**, 1888–1902.e21 (2019).
107. L. Zappia, A. Oshlack, Clustering trees: A visualization for evaluating clusterings at multiple resolutions. *GigaScience* **7**, giy083 (2018).
108. E. Galliano, E. Franzoni, M. Breton, A. N. Chand, D. J. Byrne, V. N. Murthy, M. S. Grubb, Embryonic and postnatal neurogenesis produce functionally distinct subclasses of dopaminergic neuron. *eLife* **7**, e32373 (2018).
109. C. M. Hempel, K. Sugino, S. B. Nelson, A manual method for the purification of fluorescently labeled neurons from the mammalian brain. *Nat. Protoc.* **2**, 2924–2929 (2007).
110. I. C. Macaulay, M. J. Teng, W. Haerty, P. Kumar, C. P. Ponting, T. Voet, Separation and parallel sequencing of the genomes and transcriptomes of single cells using G&T-seq. *Nat. Protoc.* **11**, 2081–2103 (2016).
111. N. L. Bray, H. Pimentel, P. Melsted, L. Pachter, Near-optimal probabilistic RNA-seq quantification. *Nat. Biotechnol.* **34**, 525–527 (2016).
112. D. J. McCarthy, K. R. Campbell, A. T. Lun, Q. F. Wills, Scater: Pre-processing, quality control, normalization and visualization of single-cell RNA-seq data in R. *Bioinformatics* **33**, 1179–1186 (2017).
113. J. Ninkovic, L. Pinto, S. Petricca, A. Lepier, J. Sun, M. A. Rieger, T. Schroeder, A. Cvekl, J. Favor, M. Götz, The transcription factor Pax6 regulates survival of dopaminergic olfactory bulb neurons via crystallin αA. *Neuron* **68**, 682–694 (2010).
114. K. Shekhar, S. W. Lapan, I. E. Whitney, N. M. Tran, E. Z. Macosko, M. Kowalczyk, X. Adiconis, J. Z. Levin, J. Nemesh, M. Goldman, S. A. McCarroll, C. L. Cepko, A. Regev, J. R. Sanes, Comprehensive classification of retinal bipolar neurons by single-cell transcriptomics. *Cell* **166**, 1308–1323.e30 (2016).
115. J. C. Burns, M. C. Kelly, M. Hoa, R. J. Morell, M. W. Kelley, Single-cell RNA-seq resolves cellular complexity in sensory organs from the neonatal inner ear. *Nat. Commun.* **6**, 8557 (2015).
116. S. McInturff, J. C. Burns, M. W. Kelley, Characterization of spatial and temporal development of Type I and Type II hair cells in the mouse utricle using new cell-type-specific markers. *Biology open* **7**, bio038083 (2018).
117. B. R. Shrestha, C. Chia, L. Wu, S. G. Kujawa, M. C. Liberman, L. V. Goodrich, Sensory neuron diversity in the inner ear is shaped by activity. *Cell* **174**, 1229–1246.e17 (2018).
118. G. La Manno, D. Gyllborg, S. Codeluppi, K. Nishimura, C. Salto, A. Zeisel, L. E. Borm, S. R. W. Stott, E. M. Toledo, J. C. Villaescusa, P. Lönnerberg, J. Ryge, R. A. Barker, E. Arenas, S. Linnarsson, Molecular diversity of midbrain development in mouse, human and stem cells. *Cell* **167**, 566–580.e19 (2016).
119. M. S. Cembrowski, M. G. Phillips, S. F. DiLisio, B. C. Shields, J. Winnubst, J. Chandrashekar, E. Bas, N. Spruston, Dissociable structural and functional hippocampal outputs via distinct subiculum cell classes. *Cell* **173**, 1280–1292.e18 (2018).
120. M. Chevée, J. De Jong Robertson, G. H. Cannon, S. P. Brown, L. A. Goff, Variation in activity state, axonal projection, and position define the transcriptional identity of individual neocortical projection neurons. *Cell Rep.* **22**, 441–455 (2018).
121. R. A. Romanov, A. Zeisel, J. Bakker, F. Girach, A. Hellysaz, R. Tomer, A. Alpár, J. Mulder, F. Clotman, E. Keimpema, B. Hsueh, A. K. Crow, H. Martens, C. Schwindling, D. Calvigioni, J. S. Bains, Z. Máté, G. Szabó, Y. Yanagawa, M.-D. Zhang, A. Rendeiro, M. Farlik, M. Uhlén, P. Wulff, C. Bock, C. Broberger, K. Deisseroth, T. Hökfelt, S. Linnarsson, T. L. Horvath, T. Harkany, Molecular interrogation of hypothalamic organization reveals distinct dopamine neuronal subtypes. *Nat. Neurosci.* **20**, 176–188 (2017).
122. A. Furlan, G. La Manno, M. Lübke, M. Häring, H. Abdo, H. Hochgerner, J. Kupari, D. Usoskin, M. S. Airaksinen, G. Oliver, S. Linnarsson, P. Ernfors, Visceral motor neuron diversity delineates a cellular basis for nipple- and pilo-erection muscle control. *Nat. Neurosci.* **19**, 1331–1340 (2016).
123. D. Usoskin, A. Furlan, S. Islam, H. Abdo, P. Lönnerberg, D. Lou, J. Hjerling-Leffler, J. Haeggström, O. Kharchenko, P. V. Kharchenko, S. Linnarsson, P. Ernfors, Unbiased classification of sensory neuron types by large-scale single-cell RNA sequencing. *Nat. Neurosci.* **18**, 145–153 (2015).
124. M. Haring, A. Zeisel, H. Hochgerner, P. Rinwa, J. E. T. Jakobsson, P. Lönnerberg, G. L. Manno, N. Sharma, L. Borgius, O. Kiehn, M. C. Lagerström, S. Linnarsson, P. Ernfors, Neuronal atlas of the dorsal horn defines its architecture and links sensory input to transcriptional cell types. *Nat. Neurosci.* **21**, 869–880 (2018).
125. A. T. Lun, K. Bach, J. C. Marioni, Pooling across cells to normalize single-cell RNA sequencing data with many zero counts. *Genome Biol.* **17**, 75 (2016).

Acknowledgments: We thank members of the Datta lab, J. Schwob, B. Sabatini, A. Schaefer, K. Franks, M. Greenberg, and V. Ruta for helpful comments on the manuscript. We thank J. Lipscombe and A. Crespo for technical support. **Funding:** S.R.D. was supported by grants RO11DC016222 and U19 NS112953 from the NIH and by the Simons Collaboration on the Global Brain, and the HMS Neurobiology Imaging Facility was supported by NIH grant P30NS072030. D.H.B. was supported by an NSF Graduate Research Fellowship. J.N. was supported by NIH grant RO1DC007235. D.R. was supported by Programma per Giovani Ricercatori Rita Levi Montalcini granted by the Italian Ministry of Education, University, and Research. K.V.d.B. is a postdoctoral fellow of the Belgian American Educational Foundation (BAEF) and was supported by the Research Foundation Flanders (FWO), grant 1246220N. D.D. was a fellow of the Berkeley Institute for Data Science, funded in part by the Gordon and Betty Moore Foundation (grant GBMF3834) and the Alfred P. Sloan Foundation (grant 2013-10-27). M.L. and M.S.G. were supported by a Leverhulme Trust Research Grant (RPG-2016-095) and a Consolidator Grant from the European Research Council (725729; FUNCOPLAN). J.M. was supported by a Medical Research Council grant (K013807) and a Medical Research Council Clinical Infrastructure Award (M008924). I.C.M. was supported by a BBSRC New Investigator Grant (BB/P022073/1) and the BBSRC National Capability in Genomics and Single Cell Analysis at Earlham Institute (BB/CCG1720/1). B.J.G. was supported by grant R01DC016859. H.M. was supported by grants R01DC014423 and R01DC016224. **Author contributions:** D.H.B., T.T., R.C., H.-J.C., R.B.F., Y.G.C., M.L., I.C.M., R.A.H., and B.J.G. designed and performed experiments. D.H.B., T.T., C.W., M.L., K.V.d.B., B.G., R.C., H.-J.C., D.D., K.S., and H.R.d.B. performed analysis. D.R., S.D., E.P., J.M., B.J.G., M.S.G., J.N., and S.R.D. designed and supervised experiments. D.H.B., T.T., C.W., M.L., H.M., D.W.L., B.J.G., M.S.G., J.N., and S.R.D. wrote the manuscript. **Competing interests:** D.W.L. is an employee of Mars Inc. All other authors declare that they have no competing interests. **Data and materials availability:** All data needed to evaluate the conclusions in the paper are present in the paper and/or the Supplementary Materials. Reanalyzed datasets are obtained from the URLs listed in the Supplementary Materials. Raw and processed datasets generated as part of this study are available from the NCBI GEO at accessions GSE148360, GSE151346, GSE153730, and GSE151709. Additional data related to this paper may be requested from the authors.

Submitted 1 May 2020
Accepted 18 June 2020
Published First Release 24 July 2020
Published 31 July 2020
10.1126/sciadv.abc5801

Citation: D. H. Brann, T. Tsukahara, C. Weinreb, M. Lipovsek, K. Van den Berge, B. Gong, R. Chance, I. C. Macaulay, H.-J. Chou, R. B. Fletcher, D. Das, K. Street, H. Roux de Bezieux, Y.G. Choi, D. Risso, S. Dudoit, E. Purdom, J. Mill, R. A. Hachem, H. Matsunami, D. W. Logan, B. J. Goldstein, M. S. Grubb, J. Ngai, S. R. Datta, Non-neuronal expression of SARS-CoV-2 entry genes in the olfactory system suggests mechanisms underlying COVID-19–associated anosmia. *Sci. Adv.* **6**, eabc5801 (2020).

Downloaded from http://advances.sciencemag.org/ on October 30, 2020

Science Advances

Non-neuronal expression of SARS-CoV-2 entry genes in the olfactory system suggests mechanisms underlying COVID-19-associated anosmia

David H. Brann, Tatsuya Tsukahara, Caleb Weinreb, Marcela Lipovsek, Koen Van den Berge, Boying Gong, Rebecca Chance, Iain C. Macaulay, Hsin-Jung Chou, Russell B. Fletcher, Diya Das, Kelly Street, Hector Roux de Bezieux, Yoon-Gi Choi, Davide Risso, Sandrine Dudoit, Elizabeth Purdom, Jonathan Mill, Ralph Abi Hachem, Hiroaki Matsunami, Darren W. Logan, Bradley J. Goldstein, Matthew S. Grubb, John Ngai and Sandeep Robert Datta

Sci Adv **6** (31), eabc5801.
DOI: 10.1126/sciadv.abc5801originally published online July 24, 2020

ARTICLE TOOLS http://advances.sciencemag.org/content/6/31/eabc5801

SUPPLEMENTARY MATERIALS http://advances.sciencemag.org/content/suppl/2020/07/24/sciadv.abc5801.DC1

REFERENCES This article cites 107 articles, 9 of which you can access for free
http://advances.sciencemag.org/content/6/31/eabc5801#BIBL

PERMISSIONS http://www.sciencemag.org/help/reprints-and-permissions

Use of this article is subject to the Terms of Service

Science Advances (ISSN 2375-2548) is published by the American Association for the Advancement of Science, 1200 New York Avenue NW, Washington, DC 20005. The title *Science Advances* is a registered trademark of AAAS.

Copyright © 2020 The Authors, some rights reserved; exclusive licensee American Association for the Advancement of Science. No claim to original U.S. Government Works. Distributed under a Creative Commons Attribution License 4.0 (CC BY).

Downloaded from http://advances.sciencemag.org/ on October 30, 2020